Pneumatic Flap Performance for a 2D Circulation Control Airfoil, Steady & Pulsed

Gregory S. Jones

NASA LaRC

Abstract

Circulation Control technologies have been around for 65 years, and have been successfully demonstrated in laboratories and flight vehicles alike, yet there are few production aircraft flying today that implement these advances. Circulation Control techniques may have been overlooked due to perceived unfavorable trade offs of mass flow, pitching moment, cruise drag, noise, etc. Improvements in certain aspects of Circulation Control technology are the focus of this paper. This report will describe airfoil and blown high lift concepts that also address cruise drag reduction and reductions in mass flow through the use of pulsed pneumatic blowing on a Coanda surface. Pulsed concepts demonstrate significant reductions in mass flow requirements for Circulation Control, as well as cruise drag concepts that equal or exceed conventional airfoil systems.

Symbols

Ao	effective cross-sectional area of 2d model
b	airfoil 2-D span, (inches)
CC	circulation control
Cp	pressure coefficient
C	airfoil chord, (inches)
C_d	section profile-drag coefficient
C_l	section lift coefficient cn cos(α) – cn sin(α)
C_m	moment coefficient
C_n	normal force coefficient
C_T	thrust coefficient = Cμ
Cμ	momentum coefficient $= \frac{\dot{m}U_j}{q(bC)}$
CCW	circulation controlled wing
DC	duty cycle (time on/total time)
D	drag (lbf)
h	slot height of Coanda jet (inches)
H	tunnel height (inches)
I,J,K	pressure tare coefficients for balance
LE	leading edge
L	lift (lbf)
M	mach number
$\dot{m}$	mass flow (lbm/sec)
NPR	nozzle pressure ratio = P_{DUCT}/P_∞
P_f	fluid power (ft-lb/sec)
P	pressure (lbf/in^2 or lbf/ft^2)
p’	fluctuating pressure (lbf/in^2 or lbf/ft^2)
r	trailing edge radius (inches)
S	airfoil reference area (ft^2)
t	airfoil thickness (inches)
U	velocity (ft/sec)
u’	fluctuating velocity (ft/sec)
q	dynamic pressure (lbf/ft^2) $= \frac{1}{2}\rho U^2$
S	wing plan form area (ft^2)
SCFM	standard mass flow (ft^3/min) (expanded to 14.7 psia & 72^{o}F)
SPL	sound pressure level (dB)
TE	trailing edge
T	static temperature (^{o}R)
w	slot width (inches)
α	angle of attack (degrees)
δ_{jet}	Reactionary force angle (degrees)
β	Prandtl-Glauert Compressiblity $\sqrt{1-M^2}$
θ_{jet}	Coanda jet separation angle (degrees)
ε	blockage interference ratio u/U
ρ	density (lbm/ft^3)
Γ	circulation

Introduction

Recent interest in circulation control (CC) aerodynamics has increased for both military and civil applications with emphasis on providing better vehicle performance and prediction capability[1]. The history of Coanda driven circulation control has met with varying degrees of enthusiasm as the requirements for improved high lift systems continue to increase. Current lift coefficient goals for Extremely Short Take Off and Landing (ESTOL) vehicles are approaching 10 and lift to drag ratios greater than 25[2]. Personal Air Vehicles (PAV) has a field length goal of 250 feet[3]. To achieve these goals require more that what a conventional high lift system can provide. In addition to high lift and cruise drag requirements, the next generation of aircraft will need to address other issues that include weight and noise. Conventional high lift systems that use flaps and leading edge slats can be associated with significant weight and volume penalties of a typical wing assembly. These assemblies are also complex (up to 3 and 4 sub-elements) and very sensitive to location relative to the main element of the wing. The need to simplify and reduce the weight of these systems without sacrificing performance is the focus of this effort.

Coanda driven circulation control techniques generally offer high levels of lift for small amounts of blowing[4]., [5] These systems are perceived to be simpler and less weighty than conventional high lift systems. However advanced system studies of circulation control systems being applied to a modern aircraft have been limited or non-existent. So the ability to buy it's way onto an aircraft is generally unproven. Nevertheless several roadblocks to real aircraft applications reappear in every discussion of circulation control. These include, source of air (typically bleed or bypass air from the engine or added auxiliary power unit), unknown weight penalties related to the internal air delivery system, engine out conditions, drag penalty associated with blunt trailing edge, and large pitching moments associated with aircraft trim. While this is not a comprehensive list, these issues will be used as a guide in developing a CC wing for general aviation applications.

A primary objective of this effort is to evaluate the benefits of pulsed circulation control and to reduce the mass flow requirements for a given lift performances as well as reduce the cruise drag penalty associated with a large circulation control trailing edge. Secondary objectives of this study were to evaluate the dual blown pneumatic concept as a control device and to determine potential benefits of returned thrust, (i.e. thrust is lost at the engine due to bleeding mass from the engine, so how much thrust is returned to the aircraft through the wing).

NASA CC Requirements

Application of circulation control to different aircraft platforms is driven by requirements that are dictated by mission.[6] NASA's Vehicle Integration, Strategy and Technology Assessment (VISTA) office describe many of these missions. Each of the vehicle sectors within the VISTA program could benefit from circulation control technologies, but Personal Air Vehicles (PAV) and ESTOL vehicles seem to benefit the most.

Personal Air Vehicles shown in Figure 1 have characteristics that resemble general aviation vehicles but meet stiffer requirements for field length (i.e. high lift), noise signatures, and cruise efficiency (L/D). With a fresh look at point-to-point travel, NASA's PAV program will address airport infrastructure, ease of use, and reductions in the cost of travel.

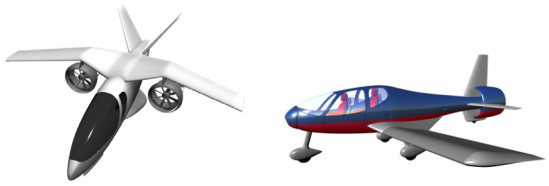

Figure 1 Notional concepts of NASA Personal Air vehicles

Today's small aircraft utilize significantly oversized wings for cruise and simple hinged flaps for high lift. These systems are adequate for the current airport infrastructure. However as

these airport requirements become more stringent, high lift and cruise efficiency must be improved. The PAV goals used for this effort included a 250' field length that will require re-sizing the wing with a C_{Lmax} =4.0 that yields an L/D_{max} of 20.

In the near-term reduced approach speeds enables a 1000' field length and can improve safety in addition to reducing community noise signatures. If equivalent control margins and gust sensitivity are achieved, safety (in terms of accident avoidance reaction time and survivability) is proportional to the approach speed. These reduced speeds require more efficient high lift systems. Circulation control technologies have been identified as a candidate simplified high lift system. It may be necessary to integrate this system with other active flow control technologies (combining higher altitude cruise, gust alleviation, limited powered-lift, etc.)

Air sources for circulation control systems for small aircraft may have a low penalty. Current high performance small aircraft are turbocharged for altitude compensation. At landing and takeoff conditions, compressed air is thrown out the waste-gate of the turbocharger (~2 lbm/sec). This is a potential source for air augmentation to a CC system. Since engine out conditions are an issue for CC applications, another air source alternative is using the wake vortex energy to power a wingtip-turbine. Regardless of the air source it is important to optimize the efficiency of the CC system for minimizing mass flow at a given lift requirement.

The NASA ESTOL vehicle sector requirements are directed to a 100-passenger class vehicle that would include the following elements:

- $\leq$ 2000' balanced field length (related goal of C_{Lmax} = 10)
- Cruise at M=0.8
- Noise footprint contained within the airport boundary
- Landing speed ~50 knots

The current state of the art aircraft systems can only achieve 2 or 3 of these elements simultaneously. Circulation control has the potential of enabling the achievement of all the elements of the desired capability set and could be integrated to the high lift, flight controls, and propulsion systems as shown in Figure 2.

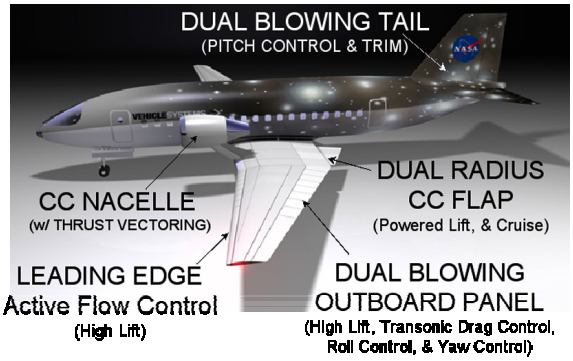

Figure 2 Notional concept of NASA ESTOL 100 passenger vehicle showing potential CC applications

It is recognized that the integration of the propulsion system and the wing is paramount to the success of either of these vehicle concepts. The focus of this paper will be targeted at a 2D baseline CC airfoil proposal that could be applied to the outer wing panel of either concept.

Theoretical Considerations

2D aerodynamic performance is traditionally categorized into lift, drag, and pitching moment. Most fluid mechanic devices that alter the forces on a body are characterized in two force categories:

- Induced forces due to circulation
- Reaction forces due to jet momentum

This section will focus on lift and drag forces associated with active flow control systems that utilize pneumatic flow control. Pneumatic or blown active flow control systems can be related to boundary layer control and/or supercirculation modes. These modes are often characterized by the fluidic power required to achieve the performance augmentation.

To achieve the maximum performance on body, it is desired to drive the stagnation streamlines toward the equivalent inviscid solution.[7] Practically this is achieved by moving the

boundary layer separation to the trailing edge. This is the performance limit for boundary layer control techniques. To achieve supercirculation it is necessary to extend the effective trailing edge beyond the physical trailing edge location with a virtual or pneumatic flap as simulated in Figure 3

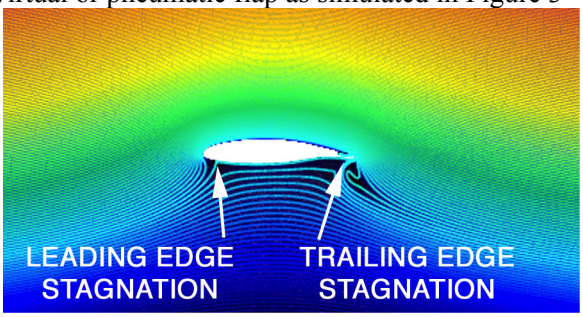

Figure 3 CFD simulation of pneumatic flap and streamline tuning using a Coanda jet

To understand the limits of airfoil performance, it in necessary to be aware of the invisid characteristics of lift. The influence of the airfoil thickness on the maximum theoretical invisid lift coefficient (not including jet thrust or camber effects) can be described as:

$$C_{L_{MAX}} = 2\pi\left(1+\frac{t}{C}\right) \qquad \text{Equation 1}$$

For a limiting case of t/C of 100% (i.e., circular cylinder) the maximum lift coefficient is 4π and can be related to classic un-blown circulation (Γ_C) around the body[8].

$$L = \rho U \Gamma_c \qquad \text{Equation 2}$$

The magnitude of the circulation (Γ_C) is a function of geometry alone and will be referred to as induced lift and can be related to the modified pressure on the integrated boundary of the body.

$$L = -\int_0^{2\pi} pr(\sin\theta)d\theta \qquad \text{Equation 3}$$

Recall for an invisid solution (circular cylinder) the normal force is solely directed in the vertical plane and that drag is zero. As seen in **Figure 4** the streamlines are significantly influenced by the magnitude of the circulation Γ_C. In practice, the inviscid limit is never reached because of flow separation. However for an airfoil employing a boundary layer control or a circulation control device, the maximum invisid lift is possible.

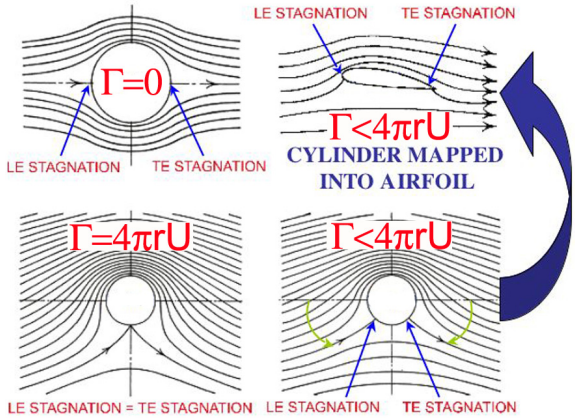

Figure 4 Classic lift due to circulation for a circular cylinder and mapped into airfoil profile

When a pneumatic system that adds mass is used, an additional circulation term is added to the induced circulation to account for the reactionary forces produced by the jet as describe in equation 4.

$$L = \rho U(\Gamma_C + \Gamma_{jet}) \qquad \text{Equation 4}$$

where $$\Gamma_{jet} = \frac{\dot{m}U_{jet}}{\rho U_\infty}(\alpha+\delta) \qquad \text{Equation 5}$$

and can be related to lift and drag as:

$$C_{L_{jet}} = C_T \sin(\alpha+\delta) \qquad \text{Equation 6}$$

$$C_{d_{jet}} = C_T \cos(\alpha+\delta) \qquad \text{Equation 7}$$

This reactionary force term can affect lift or drag depending on the orientation of the jet exit angle (δ_{jet}) at the boundary of the body. For pneumatic systems this reactionary force should not be confused with thrust vectoring that an articulating nozzle generates on an engine nacelle. The reactionary force that is characteristic of a pure jet flaps is at a fixed jet angle as shown in Figure 5.

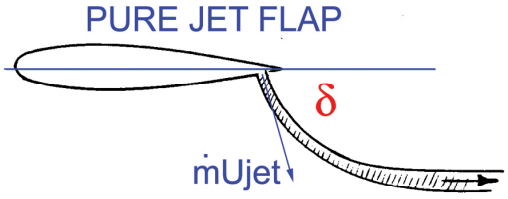

Figure 5 Thrust vectoring using a classic pure jet flap

The efficiency of a pure jet flap (vectored vertical), compared to typical CC airfoils (vectored tangential to the upper surface) is realized in the airfoil profile and the associated induced effects that accompany the Coanda geometry and the leading edge shape. It is recognized that both of these airfoil techniques benefit from induced forces and reaction forces that can be correlated to jet position and orientation. Nominally the jet flap airfoils depend largely on the reaction force of the jet momentum. Coanda type CC systems capture the induced forces more efficiently and typically deliver larger lift gains that a pure jet flap.

The combined induced circulation and reactionary forces are generally captured experimentally with a balance, integrated surface pressures, and/or wind tunnel wall pressure signatures combined with wake rake pressures, The force balance is a direct measure of both induced circulation and reaction forces. Because these forces are integrated and summed at the balance the ability to decompose the induced and reactionary components is dependant on knowing the vectored force associated with the jet.

Integrated surface pressures are representative of induced circulation forces alone. To obtain the total forces along the boundary of the body, reactionary forces must be added at the appropriate δjet angle. The integrated wind tunnel wall signature and wake rake must also account for the reaction forces generated by the jet.

For typical CC systems, the jet exit is nominally directed aft, resulting in a reactionary thrust force that contributes very little to lift (except when a aft camber causes the a small δjet) as shown in Figure 6. It should be recognized that the benefit of turning the flow with the wall bounded jet along the Coanda surface is reflected in the 2D induced circulation found in the modified surface pressure field.

The reactionary force of the CC system augments the thrust produced by the primary propulsion system, Figure 7. Returning a portion of the thrust that was bled from the engine to supply the CC sub-system, reduces the overall system penalty associated with CC. The recovery of this thrust will be dependant on the efficiency of the Coanda nozzle and internal losses of the CC air delivery system, etc.

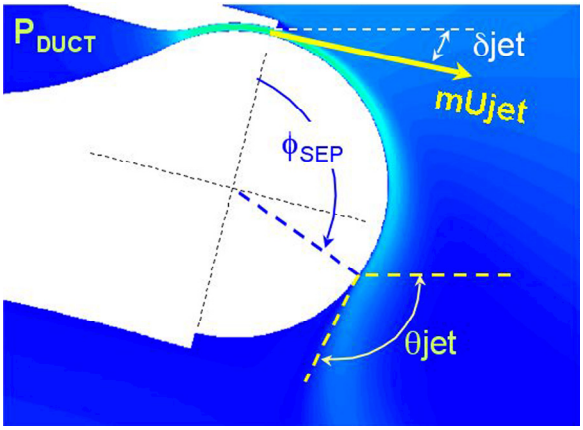

Figure 6 Schematic of flow angles associated with typical Coanda driven flow

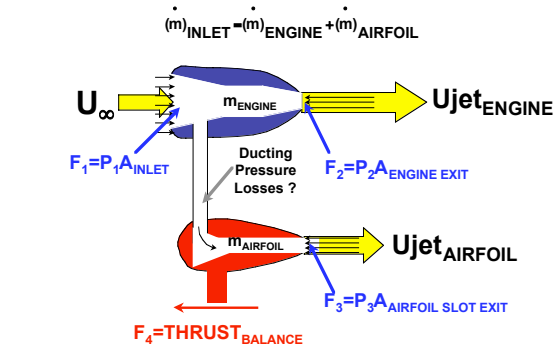

Figure 7 Block diagram of reactionary forces for an integrated wing and propulsion system

It is known that nozzle efficiency is very dependant on nozzle aspect ratio. Propulsion system studies of rectangular nozzle losses are generally limited to aspect ratios less than 10. Since there is not a data base for large aspect ratio nozzles (h/b>1300 similar to those used in CC airfoils), it would not be practical to extrapolate to obtain thrust recovery. However for this 2D study, (where nozzle aspect ratio is meaningless) it is appropriate to neglect the nozzle efficiency and assume no losses.

For 2D CC studies the thrust can be described at the jet exit of the airfoil by the momentum or

thrust coefficient:

$$C_\mu = \frac{THRUST}{qS} = \frac{\dot{m}Ujet}{qS} = \frac{2hw}{Cb}\frac{\rho_J}{\rho_\infty}\frac{U_{JET}^2}{U_\infty^2} \quad \text{Equation 8}$$

where

$$\dot{m} = \rho_J U_J (C)(w) \quad \text{Equation 9}$$

and

$$U_J = \sqrt{\frac{2\gamma R(T_{DUCT})}{\gamma - 1}\left(1 - \left(\frac{P_\infty}{P_{DUCT}}\right)^{\frac{\gamma-1}{\gamma}}\right)} \quad \text{Equation 10}$$

The trade offs of engine thrust verses reduced engine thrust augmented with CC thrust will involve detailed specifications of the geometry of the airfoil, the intake lip, internal diffusers, ducting, compressor, and jet-nozzle designs. Obviously the results would be applicable for that design only. In the absence of these details some general estimates of the benefits or penalties of CC systems can be formulated by estimating the power requirements of CC.

For a crude estimate of fluid power (P_f), it is assumed that the jet is taken from a large reservoir. Then the total power expended will be at least equal to the power required to supply the jet velocity head plus the power lost at the intake as the fluid is drawn into the large reservoir. This ideal power can be described as[9]:

$$P_f = P_{Jet} + P_{ram} \quad \text{Equation 11}$$

where

$$P_{jet} = \rho g(\Delta H)Q \cong \frac{1}{2}\rho U_J^2 \frac{\dot{m}}{\rho} \quad \text{Equation 12}$$

and

$$P_{ram} = (\rho Q U_\infty)U_\infty = \dot{m}U_\infty^2 \quad \text{Equation 13}$$

Hence, the power (ft-lb/sec) required to supply a flow with a total momentum coefficient Cμ is:

$$P_f = C_\mu \frac{U_J}{2U_\infty}\left[1 + 2\left(\frac{U_\infty}{U_J}\right)^2\right](q_\infty U_\infty S) \quad \text{Equation 14}$$

and non-dimensionally

$$C_{Pf} = \frac{P_f}{q_\infty U_\infty S} = C_\mu \frac{U_J}{2U_\infty} + C_\mu \frac{U_\infty}{U_J} \quad \text{Equation 15}$$

If the jet slot height (h) is constant and is known for a rectangular wing, the fluid power can be expressed in terms of just the parameters Cμ and height to cord ratio (h/C):

$$C_{Pf} = \frac{C_\mu^{(3/2)}}{2\sqrt{2(h/C)}}\left[1 + \frac{4(h/C)}{C_\mu}\right] \quad \text{Equation 16}$$

Figure 8 shows the non-dimensional ideal power for a typical CC jet orifice.

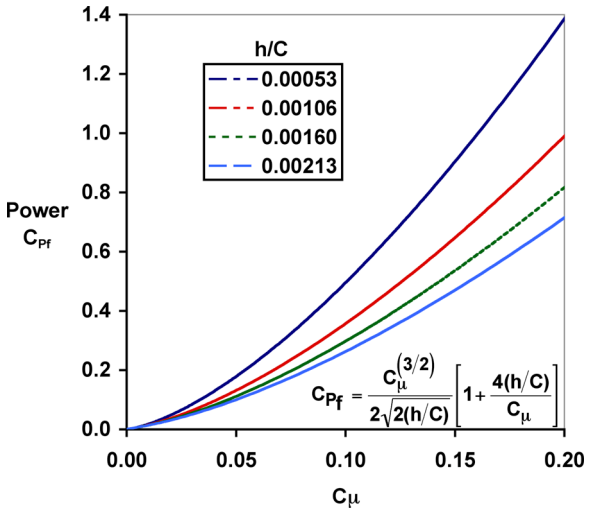

Figure 8 Ideal Power requirements for typical Coanda jets

2D Drag with Blown systems

2D drag characteristics for blown airfoils are often complicated by the juncture flow created by the wind tunnel and airfoil model. To avoid these issues the most reliable measurement technique for experimentally determining the drag of a blown airfoil is the momentum-loss method that employs a wake rake and described in detail by Betz and Jones[10]. The profile drag can be determined by integrating the wake profile[11] measured 1 to 3 chords downstream of the trailing edge.

$$C_{D_{RAKE}} = \frac{2}{c}\int\sqrt{\frac{q}{q_o}} - \frac{q}{q_o}\,dy \quad \text{Equation 17}$$

For blown airfoils, it is important to note that the measured profile drag from a wake rake must be corrected by subtracting the momentum that was added by the CC system[12]. The total horizontal forces on a 2D model do indeed exceed that indicated by conventional wake rake calculations by the quantity $\dot{m}U_o$. Considering a frictionless hypothetical case where the jet is exhausted at a total head equal to free stream total head easily confirms this principle. Here, the wake will indicate zero drag, but the model will experience a thrust of $\dot{m}U_o$. The way the net forces are book kept results in:

$$C_D = C_{D_{RAKE}} - \frac{mU_\infty}{qC} = C_{D_{RAKE}} - C_\mu \frac{U_\infty}{U_J}$$

Equation 18

This is equivalent to what a force balance would measure, assuming that the air source is considered to be internal to the model.

Equivalent Drag

To make direct comparisons of different blown systems such as traditional circulation control airfoils, jet flaps, blown flaps, engine augmented powered lift systems, etc. it is necessary to define an equivalent lift-to-drag ratio. For powered airfoil systems, the system efficiency should contain the effects of the energy that is required to obtain the airfoil performance. This also avoids the infinite efficiency that would occurs when the drag goes zero due to blowing. A correction can be made through an equivalent "kinetic energy" drag coefficient that is related to the power described above. This equivalent drag can be described as:

$$D_{EQUIV} = D_{PROFILE} + D_{POWER} + D_{RAM} + D_{INDUCED}$$

where

$D_{PROFILE}$ is the profile drag

D_{POWER} is fluid power

D_{RAM} is momentum drag force required to ingest the blowing flow rate

$D_{INDUCED}$ is induced drag (equal to zero for 2D)

For 2D flows the equivalent drag becomes:

$$D_{EQUIV} = DRAG + \frac{\dot{m}U_J^2}{2U_\infty} + \rho U_\infty \frac{\dot{m}}{\rho} \quad \text{Equation 19}$$

$$C_{DEQUIV} = C_D + C_\mu \frac{U_J}{2U_\infty} + C_\mu \frac{U_\infty}{U_J} \quad \text{Equation 20}$$

The practical implementation of the Betz or Jones wake integration techniques for blown systems are described in reference 13. When the rake drag coefficient is applied to the equivalent drag, it becomes

$$C_{DEQUIV} = C_{D_{RAKE}} + C_\mu \frac{U_J}{2U_\infty} \quad \text{Equation 21}$$

It should be noted that the kinetic energy or power that is added to the equivalent drag, dominates the equation and leads to drag values that are not practical (10,000 counts, see Figure 8) and hides the thrust generated by a typical CC airfoil..

Mass Flow Requirements

To optimize the performance of a CC system at the lowest mass flow, it is necessary to recognize the relationships between mass flow, Cμ, and slot geometry. Figure 9 highlights this relationship for a given free stream condition and geometry that is consistent with experiments described in this report. Assuming that the performance is dominated by the jet velocity ratio, reducing the slot height would result in a lower mass flow requirement.

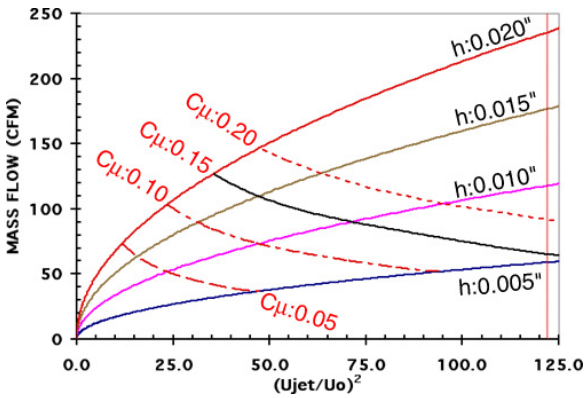

Figure 9 Mass flow requirements q=10 psf To=75°F

GACC Airfoil Design

The General Aviation Circulation Control (GACC) wing concept was initially developed for PAV[14] and is now being considered for the ESTOL concept described above. To address the requirements of PAV, the airfoil design and initial performance goals of this wing concept were to achieve:

- 2-D C_L = 3 using a simplified Coanda driven circulation control trailing edge.
- Provide a pneumatic flap capability that will minimize cruise drag and provide potential roll and yaw control (Dual blowing is defined as upper and lower Coanda surface blowing). This is based on closing the wake of the bluff trailing edge associated with typical blunt Coanda surfaces.
- Provide the capability to change the Coanda surface shape (e.g. Circular, Elliptical, and Bi-convex).
- Provide pulsed pneumatic control to minimize the mass flow requirements for high lift.
- Provide distributed flow control to customize the span-wise loading on the airfoil.

To establish a relevant circulation control airfoil geometry that is readily available to the aerodynamic community (not restricted due to proprietary issues) and that has the potential to be modified for the flight applications described above, several geometries were considered. From the late 1950's and into the 1970's, NASA has engaged in designing supercritical airfoils for transonic transport and fighter applications. These 6-series supercritical airfoils were developed to improve the cruise performance by increasing the drag rise to Mach numbers that approached 0.8[15].

The selection of the airfoil profile for this study was largely driven by the high lift requirements and with a secondary influence of cruise drag requirements. The baseline airfoil shape was initially based on un-blown wing performance. Nominally the thickness ratio has a direct effect on maximum lift, drag, stall characteristics, and structural weight[16].

The effect of airfoil thickness on lift and drag are typically counter-demanding and result in tradeoffs. For un-blown and typical CC wings the thickness ratio primarily affects the maximum lift and stall characteristics by its effect on the nose shape. For a wing of fairly high aspect ratio and moderate sweep, a larger nose radius provides a higher stall angle and a greater maximum lift coefficient.[17] However, without blowing or active flow control the drag increases with increasing thickness due to increased separation.

Wing thickness also affects the structural weight of the wing. "Statistical equations for wing weight show that the wing structural weight varies approximately inversely with the square root of the thickness ratio. Halving the thickness ratio will increase wing weight by about 41%. The wing is typically 15% of the total empty weight, so halving the thickness ratio would increase empty weight by about 6%[17]." Another benefit of a thick airfoil is the increase volume for fuel. The tradeoffs of thickness ratios will not be discussed in this paper, but the larger thickness ratio will be pursued based on the trends of maximum lift and the ability of the CC system to manage the separation issues related to large streamline turning at high lift conditions.

Therefore it was desired to combine a typical supercritical section with Coanda type CC trailing edges. Several key design for a CC airfoil are:

1. A large leading-edge radius is used to alleviate the large negative peak pressure coefficients and can be used as a substitute for a mechanical leading edge device by delaying leading edge separation and airfoil stall to high angles of attack.
2. The airfoil was contoured to provide an approximate uniform chord-wise load distribution near the design lift coefficient of 0.4.
3. A blunt trailing edge was provided with the upper and lower surface slopes approximately equal to moderate the upper surface boundary layer separation and pressure recovery and thus postpones the stall.

The NASA LS(1)-0417 airfoil is popularly known as the GA(W)-1 airfoil. Test results for the GA(W)-1 show that Cl_{max} for this type airfoil is approximately 30% greater than a typical NACA 6-series airfoil and a L/D at C_l-0.9 was about 50% greater. This 17-percent-thick supercritical airfoil[18] was chosen as a baseline geometry for the general aviation circulation control airfoil (GACC)[19] because of it's blunt leading edge, large thickness ratio, and potential to be easy to apply active flow control for transonic speeds as shown in Figure 10. It is recognized that leading

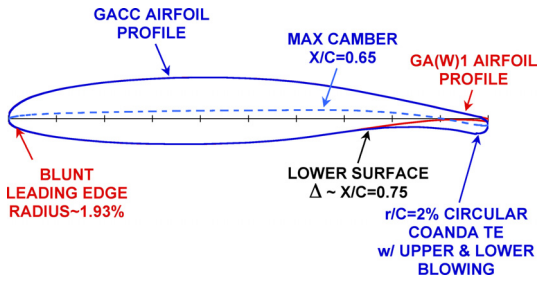

Figure 10 17 percent Thick General Aviation Circulation Control (GACC) profile with circular trailing edge

edge separation will become a problem as the leading edge stagnation moves aft. For large leading edge radius airfoils this problem occurs beyond the target lift coefficients of 3 so leading edge control will not be addressed for this study.

It was decided to modify the GA(W)-1 with Coanda type trailing edges by altering only the aft lower section of the original airfoil. The original GA(W)-1 chord line was used as the reference for AOA on the GACC airfoil design as shown in Figure 10.

The tradeoffs of sizing the Coanda surface can be related to optimizing the lift and drag for high lift or cruise conditions[20,21]. Nominally a larger trailing edge Coanda radius of curvature would lead to a higher CC lift coefficient as well as a higher cruise drag due to an increase in the trailing edge diameter. The shaded area shown in Figure 11 highlights the region of effective Coanda turning and proven lift performance highlighted by the A-6/CCW flight demonstrator[7]. The A-6/CCW airfoil[22] was a 6% thick supercritical wing section that incorporated a state-of-the-art large circular trailing edge radius of 3.67 percent chord. This large trailing edge was to guarantee a successful flight demonstration

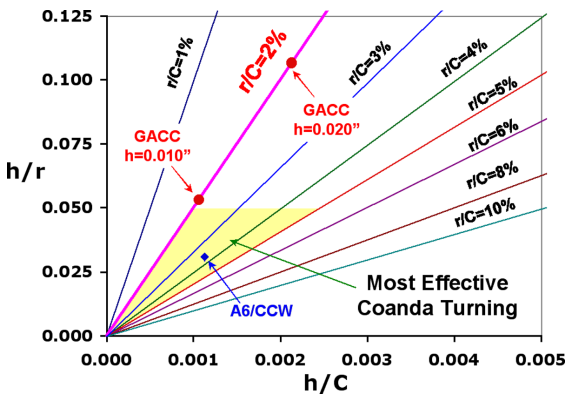

Figure 11 Effective Coanda performance for different radius and jet slot heights

of the high lift system[23] only. Any operational use of this design would require a mechanical retraction of the CC system into the wing to avoid a large cruise drag penalty.

To minimize the GACC airfoil drag performance without the use of a mechanical system a dual blowing pneumatic concept with a small radius trailing edge was designed. A baseline circular r/C of 2% was chosen for the GACC.

Three different trailing edge shapes were designed to be interchangeable and integrate with the GACC model as shown in. Figure 12 The distance between the slots remained fixed and

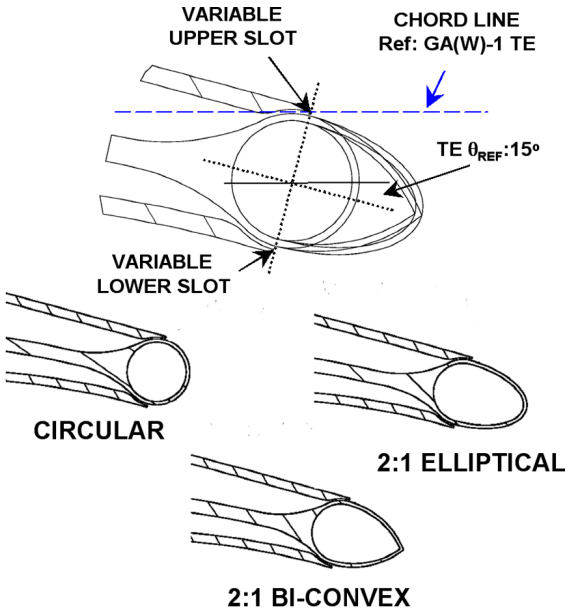

Figure 12 Sketch of interchangeable trailing edge shapes for the GACC airfoil

used the circular shape as a baseline. Both the elliptic and bi-convex shapes extended the chord by 1% (0.174"). The 2:1 elliptic shape reduced the r/C to 1% and the bi-convex shape had an r/C of 0.

To compare steady, pulsed, and dual blowing using a common model required careful design of the internal flow path as shown in Figure 13. The

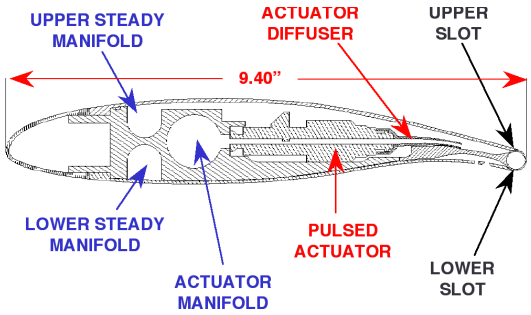

Figure 13 Sketch of internal flow path of the GACC airfoil

ability to independently control the upper and lower slot flow enables the investigation of both positive and negative lift as well as drag and thrust for both high lift and cruise conditions. A pulsed actuator system was integrated into the upper plenum of the model for investigation of unsteady circulation control.

To obtain a uniform flow path and create a 2D flow environment at the Coanda surface it was necessary to carefully design the internal flow path of all three air sources in the model as shown in Figure 14. 20 actuators were distributed in the upper plenum along the span to optimize the

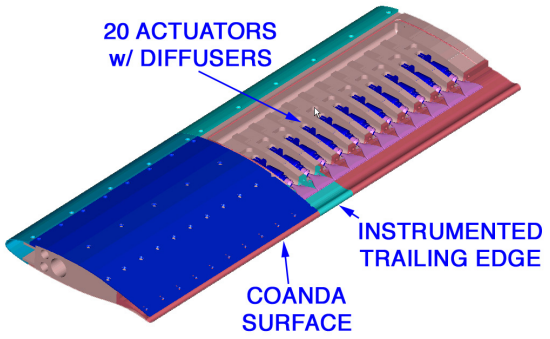

Figure 14 Sketch of GACC model with upper skin removed to highlight the flow path and instrumentation of the upper plenum.

pulsed authority to the upper Coanda jet for the high lift mode. Air for all three sources was fed from one end of the model and was expanded into large plenums then channeled to the trailing edge jet exit. Both the upper and lower slots were adjustable ($0.005 < h < 0.025$) and were fed from a smooth contraction that had a minimum area ratio of 10.

It is difficult to create an infinite or 2D environment with a fixed wall wind tunnel for blown airfoil systems. One must consider the relative size of the model to the size of the test section and the expected trajectory of the jet created by the blown system. To minimize the impact of the wind tunnel interference for CC systems, several experimental design considerations were considered:

- Solid Blockage (physical chord and span related to wind tunnel cross section)
- Wake Blockage (how much streamline turning will be achieved with blown system)
- Juncture flow regions (aspect ratio of model)

The GACC model was sized and built for the NASA LaRC Basic Aerodynamic Research Tunnel (BART) and had a chord to test section height ratio of 0.23, an aspect ratio of 3 based on a chord of 9.4 inches and a 2D wall-to-wall span of 28 inches. These values are conservative for the unblown configuration[24], however once blowing is applied the influence of the Coanda jet on streamline turning could be significant. A 2D RANS code (FUN2D) was used to evaluate the streamline turning related to Coanda blowing and super-circulation high lift conditions[19]. The free air results of this preliminary CFD evaluation indicated streamline turning and wake deflection would not impact the tunnel walls for the BART test conditions but would be influenced by the presence of the solid tunnel walls. The study of wall interference is ongoing for this experiment.

Experimental Setup

Experimental results have been obtained for a General Aviation Circulation Control (GACC) airfoil in the open return Langley Basic Aerodynamic Research Tunnel as seen in figure 15. The tests were conducted over a Mach

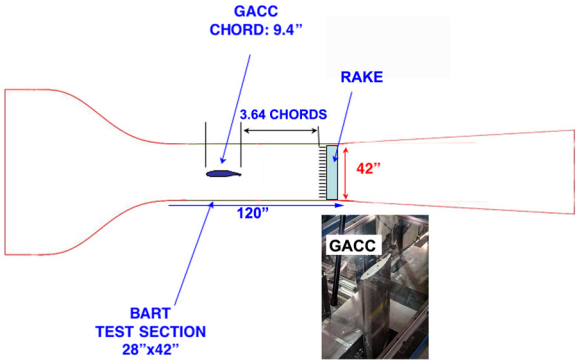

Figure 15 Sketch of the GACC setup in the Basic Aerodynamic Research Tunnel

number range of 0.082 to 0.116 corresponding to dynamic pressures of 10 psf and 20 psf respectively. Lift, drag, pitching moment, yawing moment, and rolling moment measurements were obtained from a 5-component strain gage balance. Drag data were also obtained from a wake rake. Airfoil surface pressure measurements (steady and unsteady) were used to highlight boundary layer transition and separation.

A block diagram of the BART data acquisition is shown in Figure 16. To capture the transients and time dependent characteristics of the pulsed flow field two approaches were developed, arrayed thin films and miniature pressure transducers. This report will focus only on the miniature pressure transducers. The small scale of the model did not lend itself to using off the shelf pressure transducers. Custom differential pressure gages were designed and fabricated using MEMS sensors attached directly to the skins of the model leading and trailing edges. These transducers were not temperature compensated making real time calibration necessary. To keep the measured errors from exceeding 0.05% of the full scale (2 psid) a reference pressure was monitored and calibrations were performed when necessary. This was also the case with the ESP system for 10 32-port modules with ranges of 10" H_20, 1 psid, and 2.5 psid.

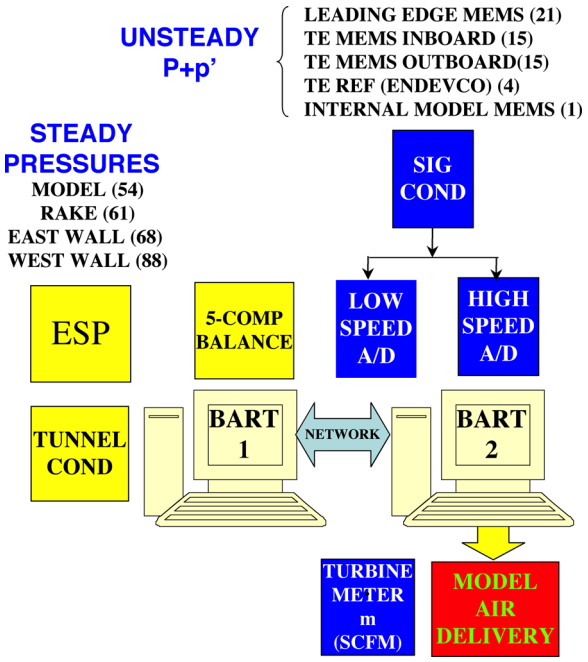

Figure 16 Block diagram of BART data acquisition for GACC setup

The 5-component strain gage balance was also custom designed and fabricated for the GACC model. Normal, axial, pitching moment (ref 50% chord), rolling moment, and yawing moment limits are shown in table 1. A drawback to the GACC balance was that the axial resonance of the balance/model system was too close to the dynamics of the loaded airfoil resulting in vibration of the model. This vibration did not always exist but led to larger than expected errors in the axial force measurement. Therefore the drag data will be reported only form the wake rake results.

Normal (lbf)	Axial (lbf)	Pitching Moment (in. lbf)	Rolling Moment (in lbf)	Yawing Moment (in. lbf)
100	10	1600	400	40

Table 1 GACC balance limits

The GACC model has three plenums that are required for use in different modes of operations, (e.g. high lift, cruise, pulsed, etc.). Each plenum

is supplied with air that is independently regulated as shown in Figure 17. To achieve the potential mass flow requirements for the largest slot area, a 2000 psia high-pressure external air source (3000 psia max) was used. The air is pre-heated to compensate for Joule Thompson effects and temperatures are maintained to within 1°R.

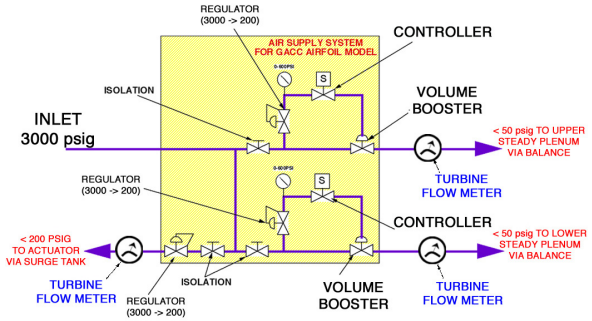

Figure 17 GACC Air delivery system

The mass flow was measured with three independent turbine meters. These flow meters are pre-calibrated and compensated for density variation at the point of measurement (accuracy=1% reading). The high-pressure plenum that supplies the pulsed actuation system is buffered with a 7.1 cubic foot air tank to eliminate the pulsed backpressure flow at the control and flow measurement station. The pressure limits of each of these systems were driven by the pressure ratio at the slot exit. Due to pressure losses in the system the upper and lower plenums were limited to 50 psid and the actuator pressure limited was 200 psid. These limits enabled sonic capability at the slot exit.

A trapeze system was used to couple the air delivery system to the model as shown in Figure 18. Special attention was given to the calibration of the balance due to the number of airlines that cross the balance. Un-pressurized calibration results are applied to a 6 x 21 calibration matrix that account for the linear interactions (1st order) and the second-degree nonlinear interactions of the balance.[25] [26] Each pressure line was then independently loaded and characterized with no flow (see appendix).

With the model mounted vertically in the tunnel the only loads experienced by the model as a result of the air delivery system were thrust loads along the span of the model. This is the same as the side-force that is not gauged or measured. The flexible hoses maintain a vertical orientation to the model and eliminate horizontal forces being applied to the balance.

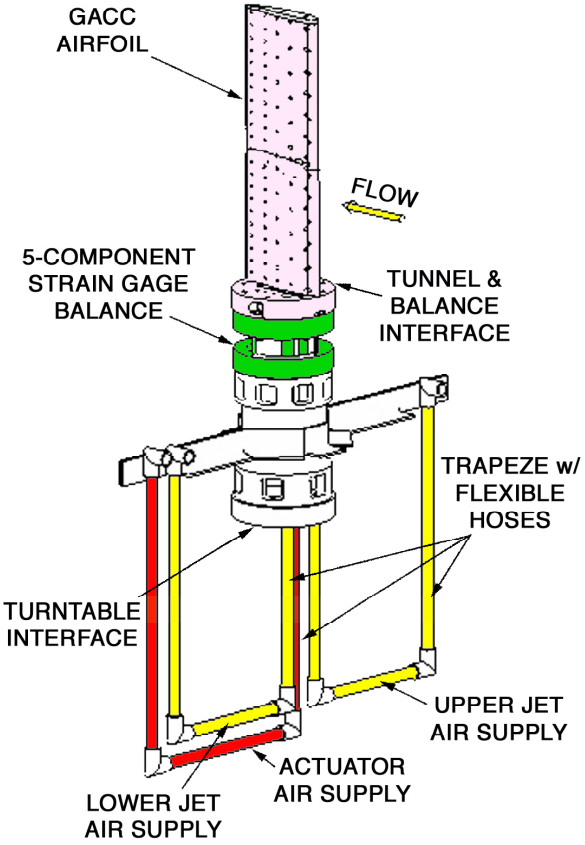

Figure 18 GACC Balance and Model interface with air delivery through trapeze system

Measurement of the drag was initially obtained with the balance and reported in reference 14. However upon careful inspection of the issues related to juncture flow interference and balance vibration, it was determined that the drag information from the balance was unreliable. A total head wake rake was designed and fabricated for the BART. The stream wise location of the rake was determined based on a balance of streamline turning (flow angle at the rake face) and the sensitivity of the pressure transducers. CFD and wind tunnel wall pressure signatures were used to identify that the jet wake was

aligned with the free stream streamlines at X/C greater than 3.5 from the trailing edge of the model. An example of the wall pressure signature is shown in **Figure 19** for typical high lift conditions.

The magnitude of the wall pressure signatures shown in Figure 19 indicates that a correction may be warranted for the dynamic pressure and angle of attack. Several wall correction techniques are described in the 1998 AGARD "Wind Tunnel Wall Corrections" report.[27] Corrections of 2-D experiments for wall effects are compounded by the 2D aspect ratio and the juncture flow of the model and wind tunnel wall interface. As a first approximation of the wall interference characteristics, corrections for 2D lift interference are made using a classic approach described in the appendix. It is recognized that these corrections

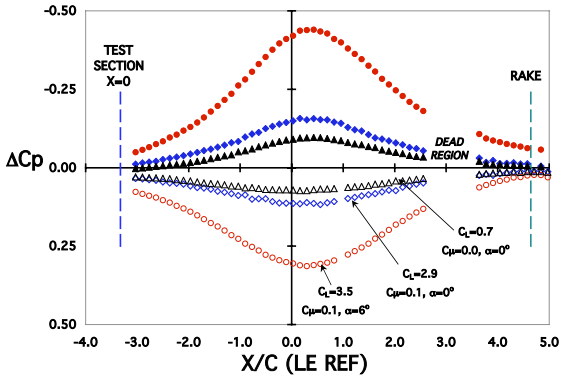

Figure 19 Wind tunnel wall pressure signatures for different lift coefficients (solid symbols for upper wall, open symbols for lower wall), h=0.020", q=10 psf, circular trailing edge

are inadequate and that wall signature method may be more appropriate. Evaluations[28] of the wall signature method are ongoing and are not applied to the data presented in this report.

The wall signature pressure distribution is also used to locate the streamwise wake rake position for this experiment. The criteria for the rake measurements are based on a tradeoff of transducer sensitivity and flow angularity of the flow at the probe tip. Based on these criteria, the wake rake was located 3.6 chords downstream of the trailing edge of the model at an angle of attack of 0 degrees. The wake profiles shown in **Figure 20** are representative of the effectiveness of the streamline turning created by the circular CC airfoil configuration. The errors associated with the integration of the wake to determine measured drag are related to the non-zero pressures outside the wake region. Even though the rake spans the entire test section only 86% is used for the wake integration, thus eliminating the influence of the floor and ceiling boundary layers. The measured drag was determined to have a repeatability of C_d=±0.0005.

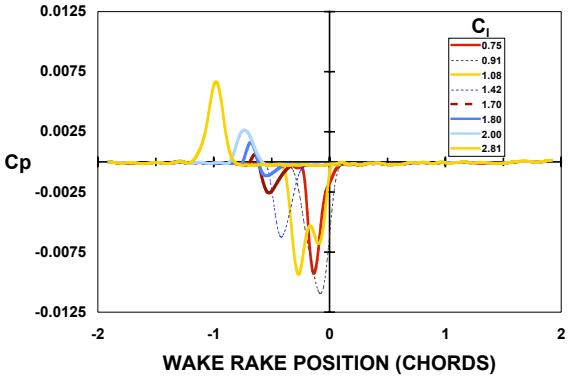

Figure 20 Wake profile of GACC with circular trailing edge, AOA=0

For the momentum sweep at AOA=0, the wake moved approximately one chord below the centerline. An example of an AOA sweep at a fixed blowing rate is shown in Figure 21. The wake moved approximately 1.5 chords below the centerline prior to stalling.

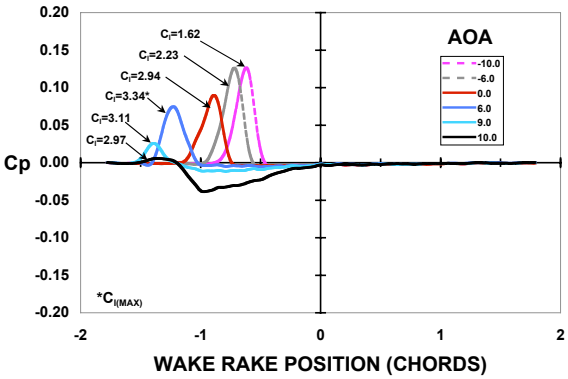

Figure 21 Wake profile of GACC with circular trailing edge, -10<AOA<10, Cμ=0.075

Errors associated with Coanda slot setup

The measurement of the non-dimensional momentum coefficient can be obtained from parameters described in Equation 8. Using mass flow and measured pressure ratios (Ujet) the momentum coefficient can be calculated without any knowledge of slot height. This is the preferred method due to the potential errors in measuring the slot height of the small-scale model used in this test. However post test evaluation of the mass flow data revealed problems with the turbine meters, requiring the use of slot height to determine the momentum coefficient.

Slot height is a critical parameter for correlation to airfoil performance and was given careful attention. Nominally the slot height was set with a digital height gage (accuracy: 0.0001") under no flow conditions. The height was then readjusted to obtain a uniform velocity along the span of the slot. The slot height was locked into place with a push-pull set of screws located approximately one inch from the slot exit inside the settling region of the jet plenum. The 0.010" trailing edge of the stainless steel skin was observed under load with a micro-telescope and did not appear to move. However, post-test span-wise jet velocities measured at the slot exit with a hot wire probe, shown in Figure 22, indicate variations of 20%

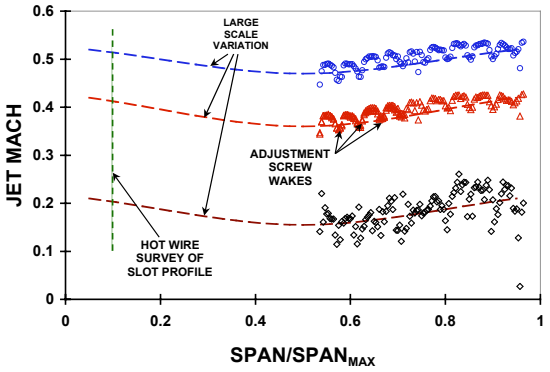

Figure 22 Example of span-wise velocity deviation for different jet exit Mach numbers (biconvex TE configuration, h=0.020")

relative to the reference jet velocity determined from pressure ratio. Most of these variations are can be identified with the wake of the internal push-pull screws used for setting slot height. The variations of the low jet velocities are larger than the higher jet velocities. It was also discovered that the extreme inboard and outboard slot velocity (not shown) was significantly lower than the core region of the span. This is attributed to internal flow separation at the inlet and exit of the flow manifold internal to the model. While affecting only the extreme 0.5" sections of the span, it does effectively reduce the length of the blowing section of the jet.

The large-scale span-wise variation is thought to be due to internal flow variations and/or errors in setting the slot height under loaded conditions. Setting the final slot height was done onsite with the model mounted in the tunnel and mass flow being added. The confined space of the small wind tunnel made setting the slot height difficult due to accessibility and noise. Pressurizing the model for maximum conditions created a jet noise and flow environment that was uncomfortable for the operator setting the slot height. Therefore a low jet velocity was chosen for the slot height adjustment process. As seen in Figure 22 there is a large scatter in the low speed jet data. This gives rise to a greater sensitivity and data scatter to the location of the measurement while setting the slot height. To compound this problem, a hand held 0.010" OD flattened pitot-probe sized to fit just inside the slot was used to make the span-wise velocity profile of the jet exit. The errors in probe location and angularity led to additional data scatter that contributed to the errors in setting slot height.

A post-test average slot height was determined using two methods; 1) a direct velocity profile and 2) conservation of mass method. During the post-test evaluation of the span-wise velocity distribution, it was discovered that the large scale Mach number variation along the span was consistent from low to high Mach numbers. Post-test hot wire measurements of the slot jet profile for the biconvex configuration are shown in Figure 23. The slot height was nominally set to

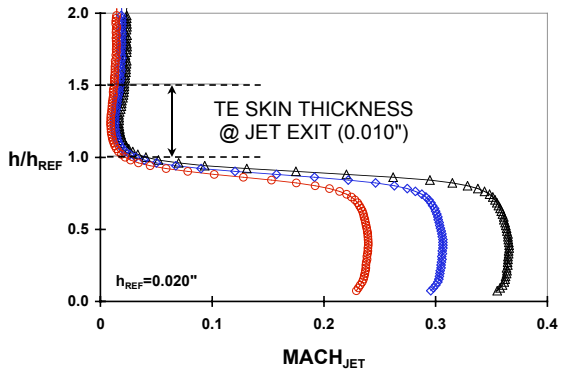

Figure 23 Example hot wire velocity profiles at the slot exit plane. Measurements are between adjustment screws at Span/Span$_{MAX}$=0.1 (biconvex TE configuration, h=0.020")

0.020". Normalizing these profiles with the velocity measured via the pressure ratio used throughout the experiment revealed that the hot wire maximum velocity results were 20 percent high as shown in Figure 24. This is consistent with the span location chosen for the velocity profiles.

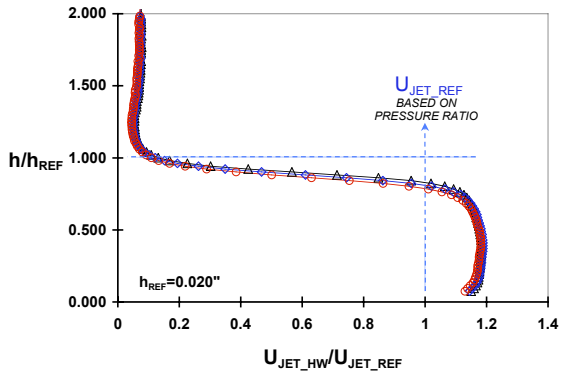

Figure 24 Normalized velocity profiles at the upper surface exit plane of the biconvex TE.

The conservation of mass method for determining slot height utilizes the integrated jet velocity determined with from the pressure ratio and the measured mass flow.

$$h = \frac{\dot{m}}{\rho_{JET} U_{JET} b} \quad \text{Equation 22}$$

Each trailing edge configuration had two targeted slot heights to be tested, h_{NOM}=0.010" and h_{NOM}=0.020". Post-test analysis revealed that the slot heights were 5 to 30 percent higher than was thought to be at the time of setup as shown in **Figure 25** for the circular trailing edge. The calculated slot height also varied up to 18 percent with increasing nozzle pressure ratio. An average

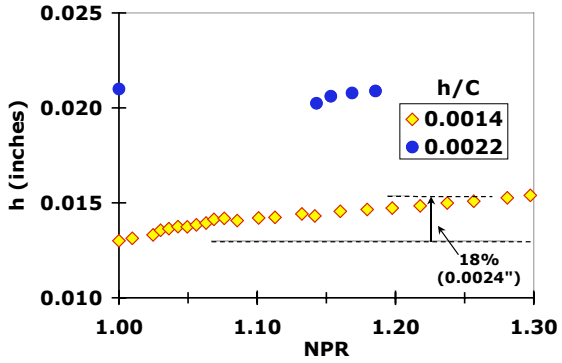

Figure 25 Slot height variation as internal plenum pressure increases for Circular TE

of slot height for the varying mass flow was used for reporting purposes. Extrapolating the biconvex calculated profile to the un-blown condition results in a 0.021" setup. This is consistent with the slot height measured in the post-test slot profile hot wire measurements shown in Figure 24.

Airfoil performance

Airfoil performance will be discussed for two modes of the GACC airfoil; the high lift mode with upper slot blowing and the cruise mode with upper and lower slot (dual) blowing. The efficiency of pulsed blowing will be discussed as part of the high lift mode.

High Lift Mode

Baseline (No Blowing)

Lift, drag, and pitching moment will be used to establish the 2D baseline performance of the GACC airfoil with different trailing edges. The original GACC airfoil was designed around the circular trailing edge having an r/C of 2%. Therefore the circular trailing edge will be used as the reference for the elliptic and biconvex trailing edges. Comparing the lift performance of the three trailing edges with no blowing in Figure 26, the circular trailing edge has a lift enhancement of $\Delta C_l = 0.16$ at a zero degree angle of attack

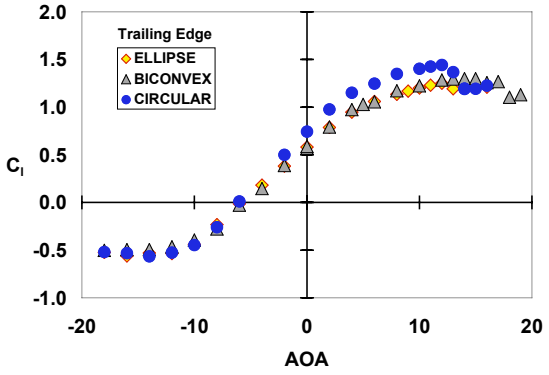

Figure 26 Baseline lift coefficient with no blowing (Balance Data)

relative to the biconvex and elliptic trailing edges. This is also reflected in the trailing edge pressures shown in Figure 27.

Comparisons of the drag performance for the three trailing edges are shown in Figure 28. There are little differences in the indicated drag. This can be related to boundary layer transition fixed at 5% chord and the fixed trailing height established by the steps created by the upper and lower slots. Minimum drag occurs at zero lift and AOA=-6.

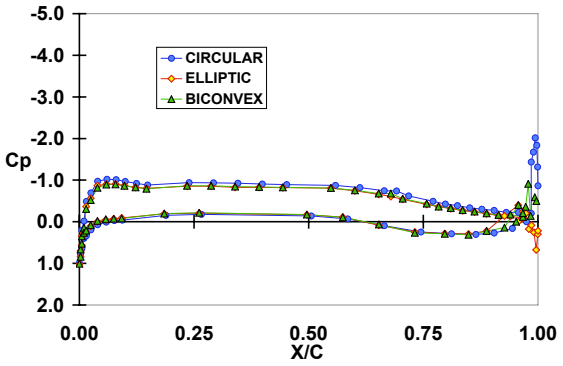

Figure 27 Pressure distribution for GACC airfoil no blowing AOA=0

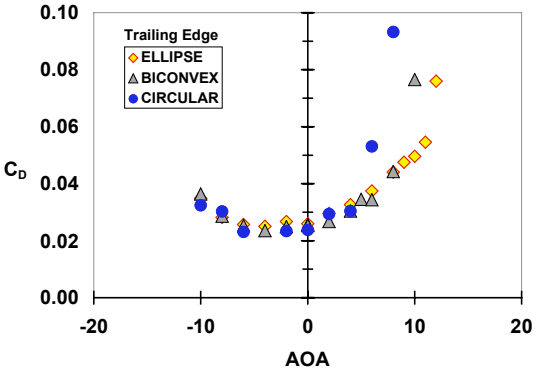

Figure 28 Baseline drag coefficient with no blowing (wake rake)

The airfoil efficiency is shown in Figure 29 indicates that the circular trailing edge is more efficient than the elliptic or biconvex trailing

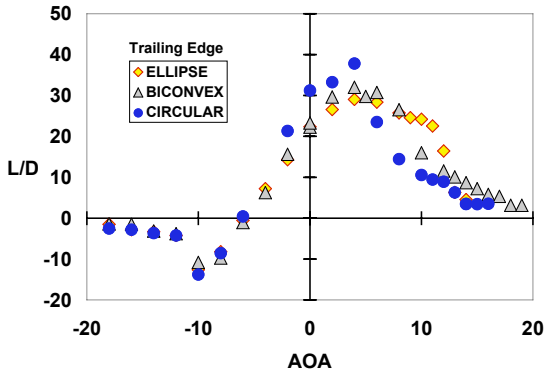

Figure 29 Baseline GACC airfoil efficiency with no blowing

edges with no blowing. The peak efficiency occurs at AOA of 6 degrees and is consistent with the differences in lift. The drag polar shown Figure 30 illustrates a relatively flat drag characteristic for the region of lift that is consistent with cruise conditions (e.g. C_l=0.5).

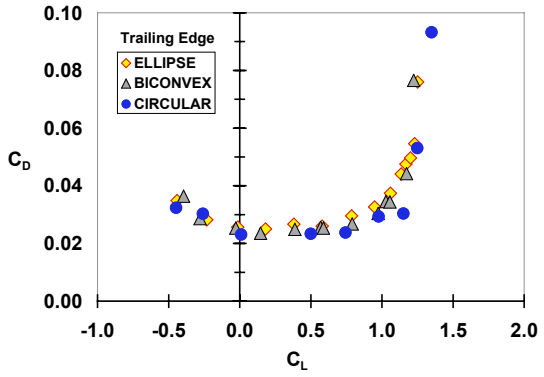

Figure 30 Baseline drag polar for GACC airfoil with no blowing

Circular Trailing Edge

The circular Coanda trailing edge will be used as a reference for comparisons of performance throughout the rest of this paper. This section will highlight the circular trailing edge performance for high lift conditions. While somewhat arbitrary, the initial goal of this effort was to generate a lift coefficient of 3 at an AOA of 0 degrees. Figure 31 illustrates that using

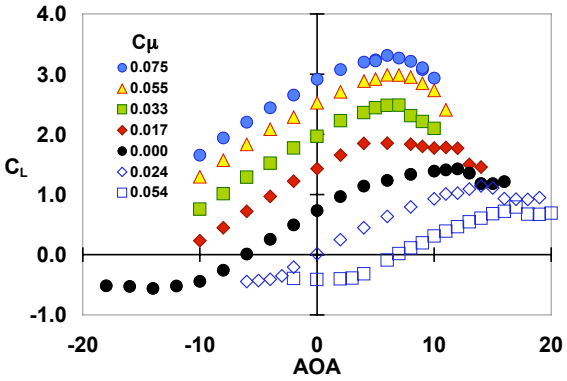

Figure 31 Airfoil lift performance with circular TE & h/C=0.0022 (Open symbols represent lower blowing)

upper Coanda blowing the target lift coefficient of 3.0 was achieved. The maximum lift that this airfoil can achieve is still undetermined, but will be limited by the leading edge performance of the airfoil. The leading edge stall characteristics of this CC airfoil are highlighted in Figure 31. These data are consistent with other supercritical CC airfoils with large leading edges.

Lower Coanda blowing gives this airfoil configuration a unique ability to manage lift and drag by generating a negative lift capability. The open symbols shown in Figure 31 highlight the lower Coanda blowing. The pneumatic flap effect of lower blowing compensates for the trailing edge camber as demonstrated by zero lift at AOA of zero ($C\mu_{LOWER}$=0.024). These effects are more related to cruise drag and will be discussed later in this paper.

The efficiency of the Coanda blowing can be related to the slot height and the radius of the Coanda surface. For a fixed Coanda surface radius of r/C=2%, an h/C of 1.4% performed better than an h/C of 2.2% as shown in Figure 32.

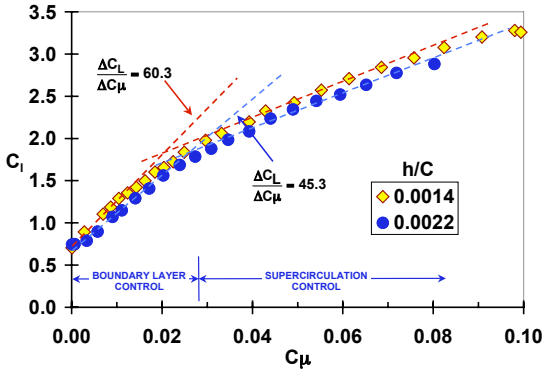

Figure 32 Lift performance of Circular TE, AOA=0

The lift augmentation for the small slot was 60.3 in the separation control regime compared to the 45.3 augmentation for the larger slot. To extend into the supercirculaiton regime it is necessary to push the rear stagnation beyond the physical trailing edge forming a pneumatic flap. A shift in the lift augmentation efficiency highlights this effect as shown in Figure 32. The limit of the separation region for this airfoil occurs at a Cμ of approximately 0.03 and a lift coefficient of 1.8. To predict the mass flow requirements and lift

performance in the supercirculation region, it is possible to extend the supercirculaiton lift augmentation line.

The drag characteristics corresponding to Equation 18 are shown in Figure 33. Thrust is generated for low blowing rates that are characteristic of most CC airfoils including GACC. Combinations of Coanda blowing and AOA allow for variable drag at a fixed lift condition. As an example, the drag can be varied by ΔCd=0.060 at a lift coefficient of 2.0, This would include both a thrust and drag capability...The limitations of this capability are related to the leading edge stall characteristics and may be augmented with leading edge active flow control.

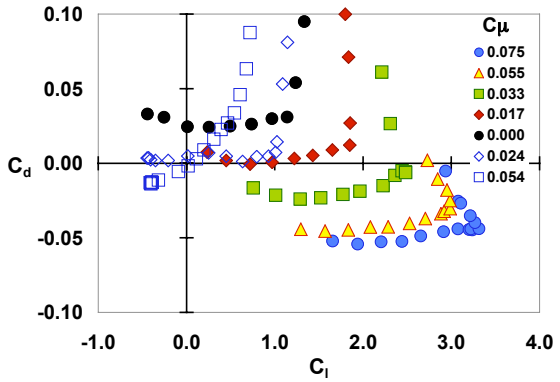

Figure 33 Airfoil drag polar for circular TE h/C=0.0022, Wake rake data (Open symbols represent lower blowing)

To gain a greater understanding of drag characteristics for this airfoil, the total drag measured in the wake can be decomposed into a 2D circulation induced force represented by the pressure distribution on the airfoil (shown in Figure 34) and the reactionary force created by the Coanda jet evaluated at the jet exit. The reactionary force and the induced force can be combined to create the total force measured. Since the total drag force is known from the wake rake data and the reactionary force C_T is equivalent to Cμ, then the 2D circulation induced force will become:

$$C_{d_{2D-INDUCED}} = C_{d_{TOTAL}} - C\mu\left[\cos(\alpha+\delta)\right]$$

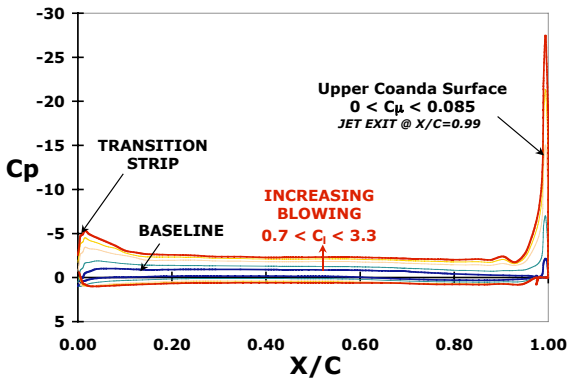

(a) Airfoil pressure distribution

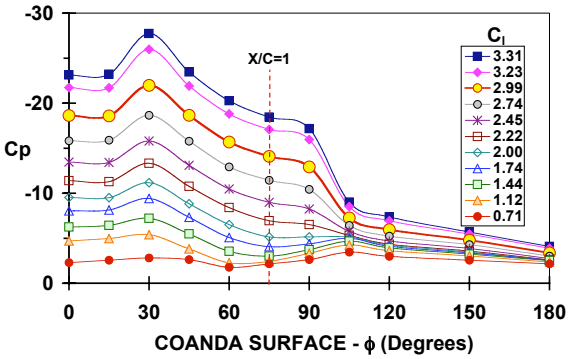

(b) Expanded view of circular trailing edge pressure distribution

Figure 34 GACC pressure distribution with circular trailing edge, AOA=0, h/C=0.00106

An example of the 2D circulation induced drag force is shown in Figure 35. This data corresponds to the lift data in Figure 32. An observation that the slope change that is related to the supercirculation region in the lift data is also evident in the drag data, occurring at a momentum coefficient of approximately 0.03. .

The efficiency of a blown airfoil has traditionally been related to an equivalent drag as described earlier in the text. The equivalent drag shown in Figure 36 highlights the conversion of measured thrust to equivalent drag for two slot configurations. While this enables the one to compare one blown system to another, it is dangerous for the designer to use these values as seen by comparing figures Figure 35 and Figure 36.

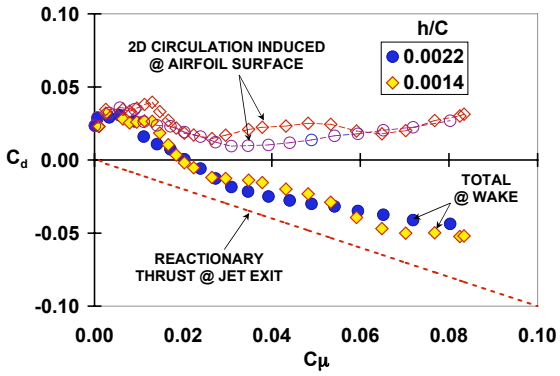

Figure 35 Drag performance of Circular TE, AOA=0

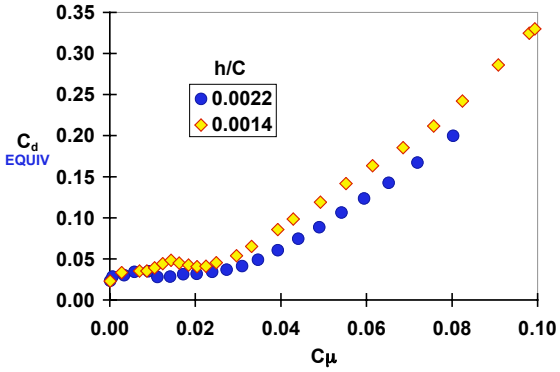

Figure 36 Equivalent drag of Circular TE, AOA=0

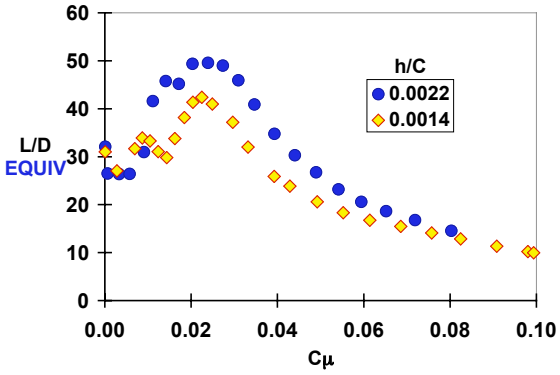

Figure 37 Efficiency of Circular TE, AOA=0

The efficiency of the airfoil can be represented by the lift to equivalent drag ratio shown in Figure 37. Comparison of the two slot configurations indicates a greater efficiency of the larger slot. This is a result of the drag benefits of the larger slot and is believed to be related to the turbulence characteristics of the Coanda jet. The peak efficiency occurs in the vicinity of the transition from boundary layer control to supercirculation (refer to Figure 35).

The 2D L/D equivalent efficiency of the airfoil can also be related to the fluidic power required of the high lift system as shown in Figure 38. The corresponding equivalent drag data are shown in Figure 39. The fluidic power can be related to the reactionary thrust component described in Figure 35. The dashed line represents the contribution of the fluidic power to the equivalent drag. Any values that deviate above or below this line can be related to the 2D circulation induced effects described above and highlight the magnitude of the dominating contribution of the fluidic power to the equivalent drag.

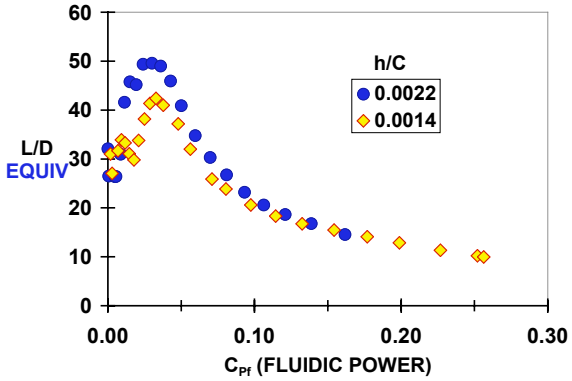

Figure 38 Pumping power required to achieve equivalent GACC airfoil efficiency for circular TE, AOA=0

Evaluating the measured drag per fluidic power reveals that the most efficient use of the fluidic power occurs in the boundary control region. This is shown in Figure 40 where $\Delta C_d/C_{Pf}$ is a minimum. The magnitude of the incremental thrust for the larger slot height is 0.9324 at a fluidic power of 0.03873 shown in Figure 41. This corresponds to a thrust of 0.0295 (reference Figure 35).

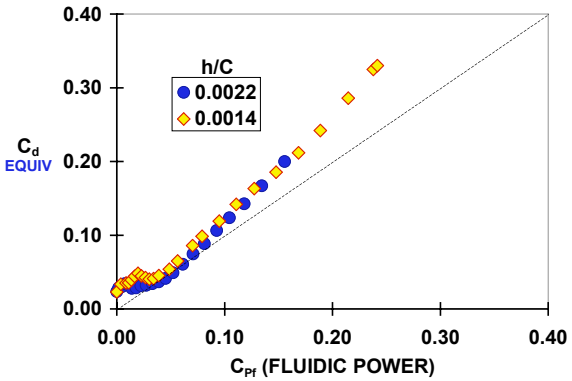

Figure 39 Fluidic power required to achieve equivalent drag for circular TE, AOA=0

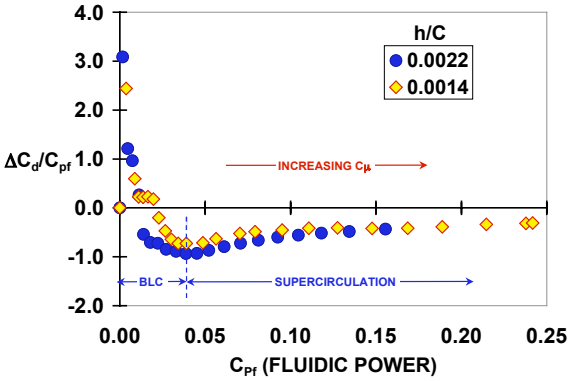

Figure 40 Drag efficiency per fluidic power for GACC airfoil with circular TE, AOA=0

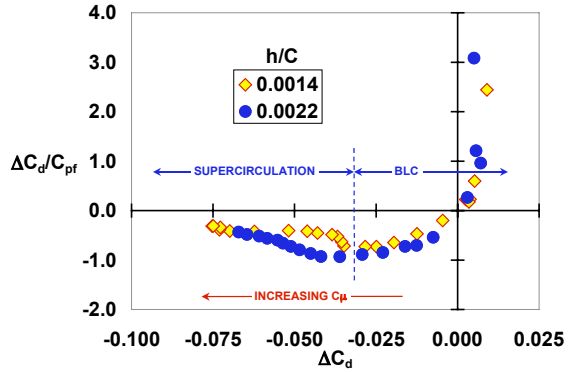

Figure 41 Drag per power ratio for GACC airfoil with circular TE, AOA=0

This also illustrates a benefit of a blown system compared to other active flow control techniques such as synthetic jets and suction systems.

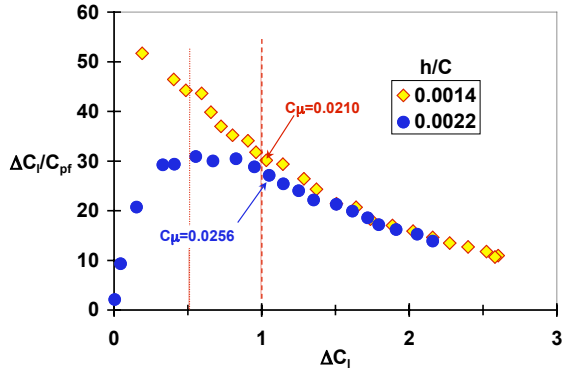

Figure 42 Lift per power ratio for GACC airfoil with circular TE, AOA=0

Without the benefit of the reactionary force of the jet, the best performance a traditional active flow control system could achieve would be related to moving or attaching the boundary layer to the to

the most aft portion of the airfoil. This would result in a theoretical zero drag. For a tangentially blown system typical of CC airfoils, the reactionary forces enable thrust to the system that is not available to unblown systems. To make a direct comparison of these different active flow control systems it would be necessary to equate the relevant power (watts, horsepower, etc.) to achieve a comparable drag performance.

Another performance parameter of interest is the lift-increment-per-power ratio, $\Delta Cl/C_{Pf}$ shown in Figure 42. This parameter is occasionally used for direct comparisons of similar power-augmented devices[9]. The comparisons are made at ΔC_l of 0.5 and 1.0, which are consistent with the boundary control region, and the initial stage of supercirculaiton. For the GACC airfoil the smaller slot develops more lift for a given power setting than the larger slot in the boundary layer control region. As the power (or momentum) is increased into the supercirculation region, the influence of slot height on lift-to-power augmentation decreases.

Comparing the power requirements for the GACC to other similar airfoils are shown in Table 1. The GACC airfoil performance is comparable to that of a similar CC airfoil and blown flaps with active flow control.

ITEM	$\Delta C_l/C_{Pf}$ (ΔC_l =0.5)	$\Delta C_l/C_{Pf}$ (ΔC_l =1.0)
GACC (h/C=0.0014)	44.3	31
ELLIPTIC CC[29]	40.4	28.6
TE BLOWN FLAP[30]	42.6	33.2
FLAP KNEE[31] (BLC Mode)	26.8	7.48

Table 1 Comparison of GACC lift increment-per-power to similar powered systems[9]

The pitching moment characteristics of the GACC airfoil are shown in Figure 43. These values are consistent with other CC airfoils.

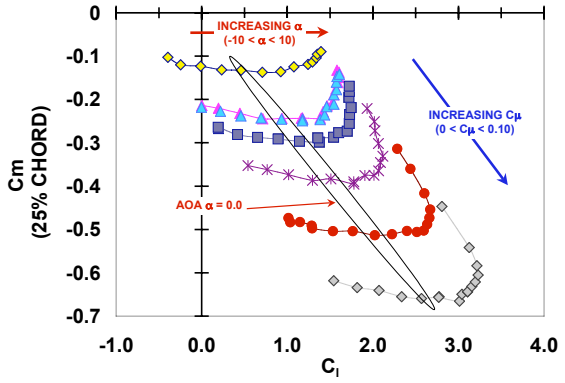

Figure 43 25% chord pitching moment characteristics of GACC, h/C=0.0022

Performance Comparisons of Trailing Edges

The following section will focus on comparisons of the different shape trailing edges with a fixed slot height of h/C=0.0022. The shapes include circular, elliptic, and biconvex profiles having effective trailing edge radius of r/C=2%, 1%, and 0% respectively. The lift performance of the larger radius configuration is higher than the other configurations as seen in Figure 44.

A comparison of the drag performance, shown in Figure 45, highlights the improvement of the drag as a function of the smaller r/C. The elliptic trailing edge (r/C=1%) has less drag than the circular trailing edge (r/C=2%) throughout the boundary layer and supercirculation region. Transitioning from the boundary layer region to the supercirculation region the total thrust of the elliptic trailing edge exceeds the reactionary thrust, implying a net 2D circulation induced thrust. The drag performance of the biconvex shape mimics the circular trailing edge performance in the boundary layer control region. The thrust for the biconvex configuration extends beyond the reactionary thrust throughout the supercirculation region.

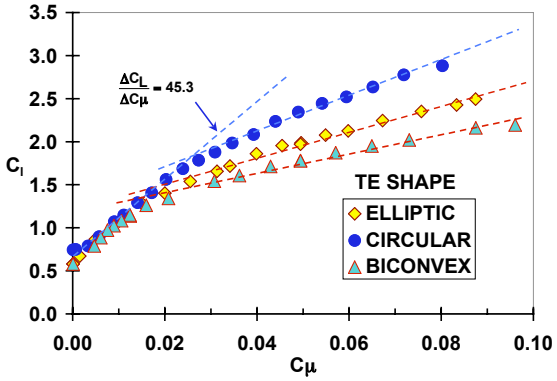

Figure 44 Comparison of lift performance for the GACC airfoil for different trailing edge shapes, h/C=0.0022

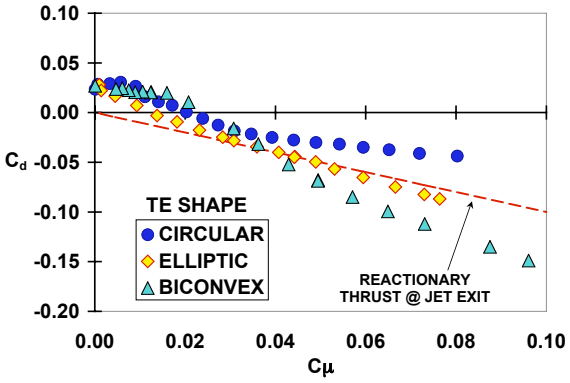

Figure 45 Comparison of the thrust performance of the GACC having three different trailing edge shapes.

Comparisons of drag polars for the three different trailing edges are shown in Figure 46. The effectiveness of the sharp trailing edge is reflected in the increased thrust for the biconvex trailing edge.

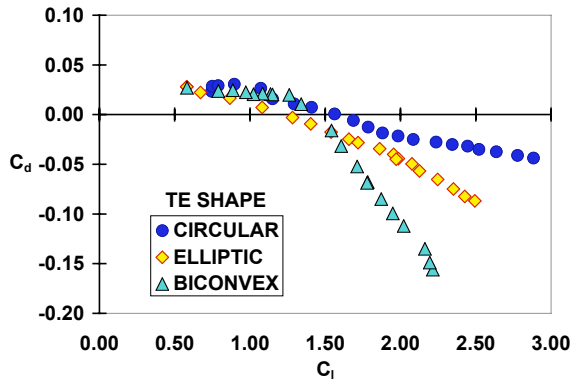

Figure 46 Comparison of drag polars for three different trailing edge shapes, h/C=0.0022

Comparisons of pitching moments for the three trailing edges are shown in Figure 47. The biconvex trailing edge has the lowest pitching moment for any given lift. The benefits of high thrust and low pitching moment comes at the price of momentum coefficient, e.g. for a lift coefficient of 2 the thrust of the biconvex is 110 counts larger and the moment is 50 counts smaller than the circular trailing edge performance. However the momentum coefficient increased by a factor of 2.

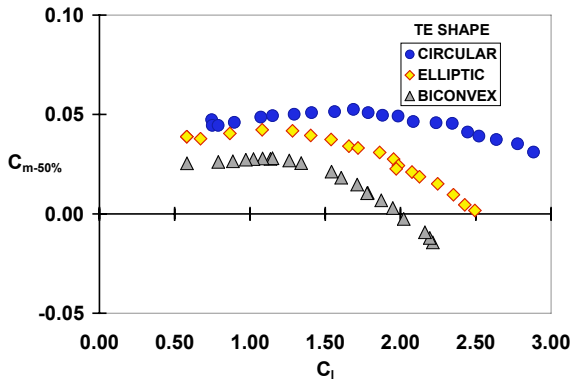

Figure 47 Comparison of pitching moments (referenced to 50% chord) for three different trailing edge shapes, h/C=0.0022

Cruise Configuration

To address the issue of a blunt trailing edge for typical CC configurations at cruise, the GACC was designed with a dual blowing capability, i.e. upper and/or lower blowing on the Coanda surface[32]., [33] This enables the operator to augment the system thrust while providing roll and/or yaw control. The following section will address only the dual blown circular trailing edge performance.

Dual Blowing for Circular Coanda surface

It should be recognized that the cruise condition for this airfoil would be operated at a substantially higher Mach number and higher dynamic pressure, thereby reducing the momentum coefficient These low speed data do not account for the airfoil compressibility and potential shock manipulation that typical CC configurations may provide. For cruise conditions the CC performance characteristics are limited to the boundary layer control region. Nominally lift coefficients that are the order of 0.5 are desired during cruise operations.

To characterize the lift performance of the dual blown configuration of the GACC airfoil, the upper blowing condition was fixed and the lower blowing was swept as shown in. Figure 48. As expected the upper blowing performance remains proportions to the lift. Combining this upper blowing with lower blowing will result in a lift reduction. However, this reduction does not

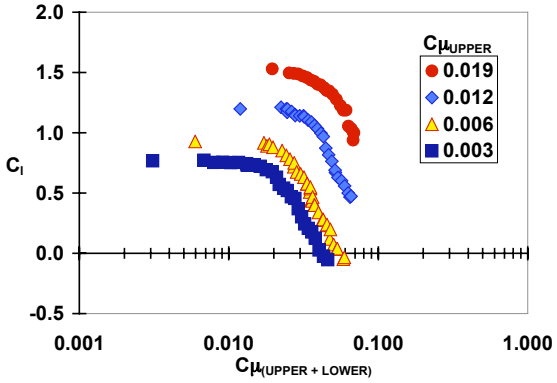

Figure 48 Lift performance for dual blowing h/C-0.0022

occur until the initial stages of thrust.

The effectiveness of the dual blown configuration is realized in the drag performance. The drag characteristics associated with Figure 48 are shown in Figure 49. The drag performance seems to be independent of upper blowing in the

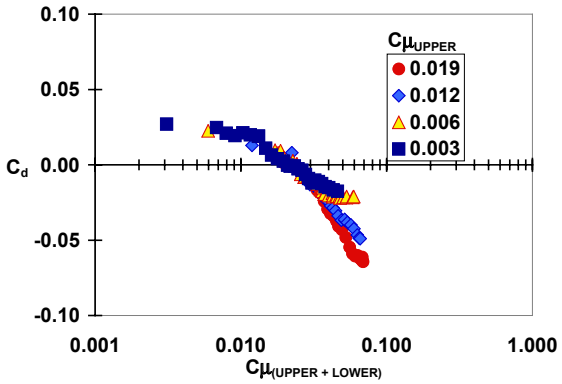

Figure 49 Drag characteristics of the circular dual blown configuration, h/C=0.0022

boundary layer control region. The drag polar, shown in Figure 50, indicates that thrust can be adjusted for a given lift. (e.g. for a fixed C_l=0.5 a ΔC_d=-0.043 can be adjusted using dual blowing).

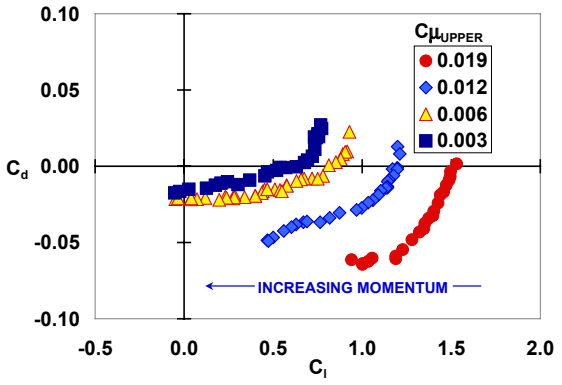

Figure 50 Drag polar for the dual blowing cruise configuration of the GACC airfoil, circular trailing edge, h/C=0.0022 (upper and lower)

The wake profile shown in Figure 51 corresponds to the fixed upper blowing of Cμ=0.003. As the lowing blowing rate increases, the profile goes from a single peak to a double peak.then returns to a single peak. This indicates that the upper and lower jets are independent and do not mix efficiently for the blunt circular trailing edge.

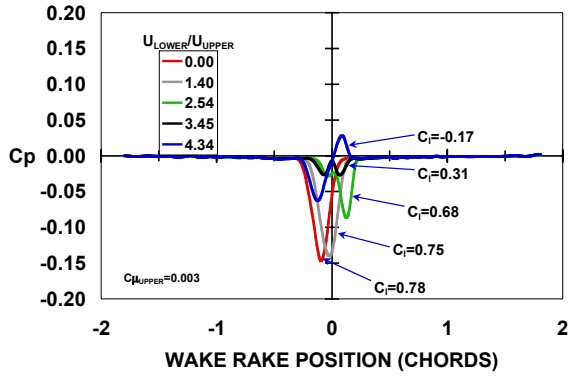

Figure 51 Wake profiles for the dual blowing cruise configuration of the GACC airfoil, circular trailing edge, reference $C\mu_{upper}$=0.003, h/C=0.0022 (upper and lower)

The equivalent drag for the circular dual blown configuration is shown in Figure 52. The minimum equivalent drag occurs at a combined momentum coefficient of 0.03 and a fixed upper momentum coefficient of 0.003. This is

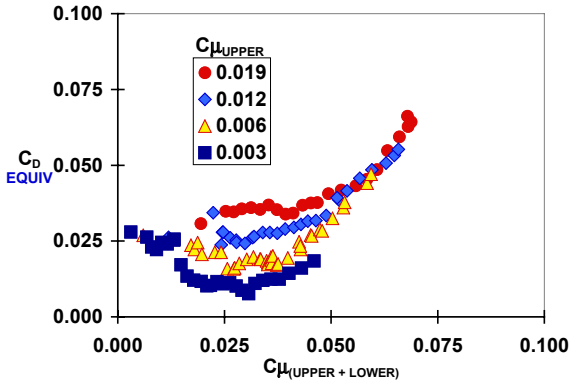

Figure 52 Equivalent drag for the GACC dual blown circular trailing edge

consistent with a measured total drag of -0.012.

The peak efficiency shown in Figure 53 occurs at a total momentum coefficient of 0.021. This is consistent with the measured drag transitioning from drag to thrust.

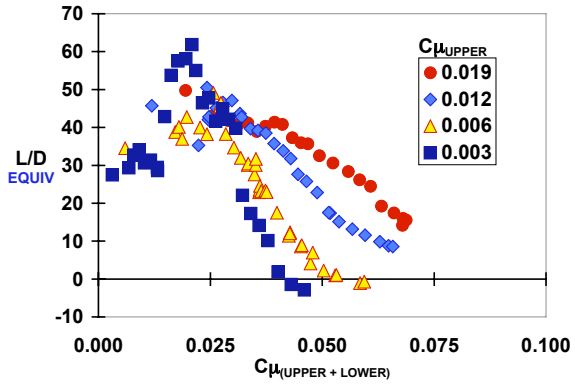

Figure 53 Airfoil efficiency for the GACC dual blown circular tailing edge

Pulsed Blowing

As will be shown in this section, pulsed blowing from the upper slot is intended to reduce the mass flow requirements for a comparable steady blowing performance.[34, 35] The GACC pulsed blowing system[19] is based on a high-speed valve that delivers a high volumetric flow to the upper jet exit. The actuator is close coupled (internally located x/C=0.90) to the jet exit through a rapid diffuser to deliver a pulse of air that can be varied in magnitude, frequency, and duty cycle. An example of the pulse train is shown in Figure 54.

.

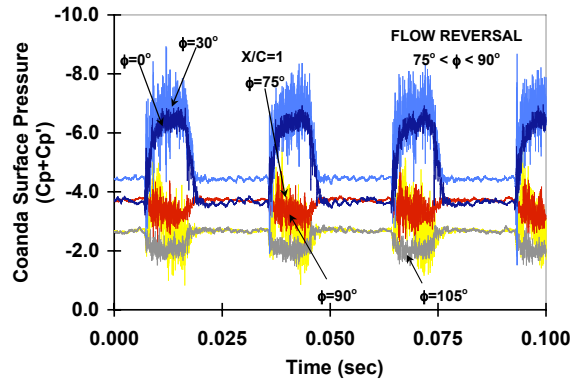

Figure 54 Time record of circular Coanda surface pressures with pulsed upper blowing, 35 Hz, 40% duty cycle, circular trailing edge h/C=0.00106.

The quality of the rise time and decay of the pulse train is related to the overall actuator authority. The rise and decay time of the pulse train is dependent on the internal volume located internally just upstream of the jet exit. This includes the 10:1 contraction and the settling area downstream of the rapid diffuser exits.

The time dependant pulse train is referenced to the jet exit or ϕ=0 of the Coanda surface. The averaged pressure field is compared to a comparable steady blowing condition, shown in Figure 55. The separation associated with this condition was identified to occur 75<ϕ<90, whereas steady blowing produced a separation

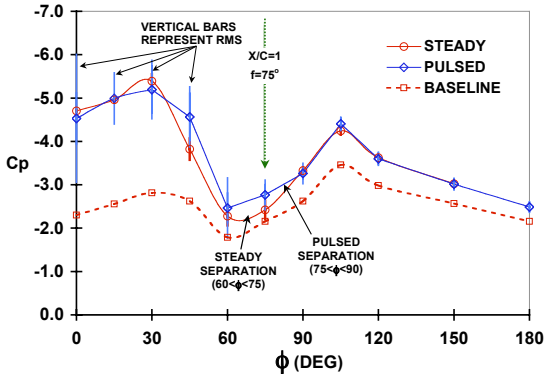

Figure 55 Comparison of steady and pulsed pressure distribution for the circular trailing edge, h/C=0.00106

60<ϕ<75. This corresponds to a lift performance shown in Figure 56. The mass flow reduction of 55% corresponds to the 40% duty cycle shown in Figure 54. It should be emphasized that this reduction is limited to the boundary layer control region due to current limits in actuator authority.

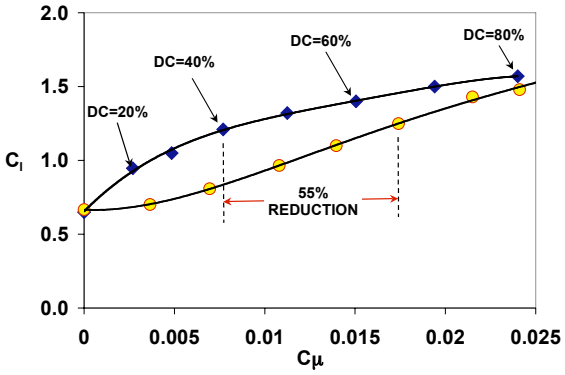

Figure 56 Comparison of lift performance for steady and pulsed blowing on the circular trailing edge, h/C=0.00106

The turbulence magnitude and frequency of the steady jet, shown in Figure 57, increases just downstream of the jet exit, then increases along the Coanda surface to peak at $\phi=30^{o}$. The magnitude and frequency then decays until the jet separates from the Coanda surface between

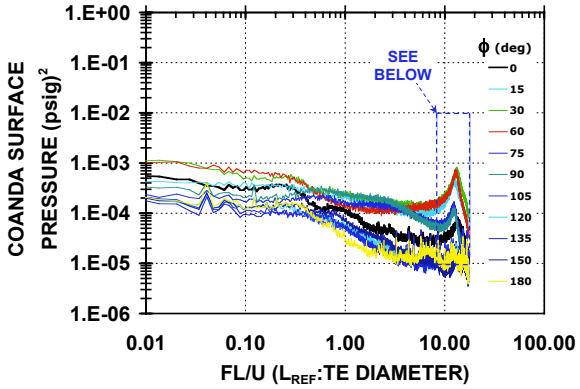

(a) Non-dimensional Spectra for steady jet

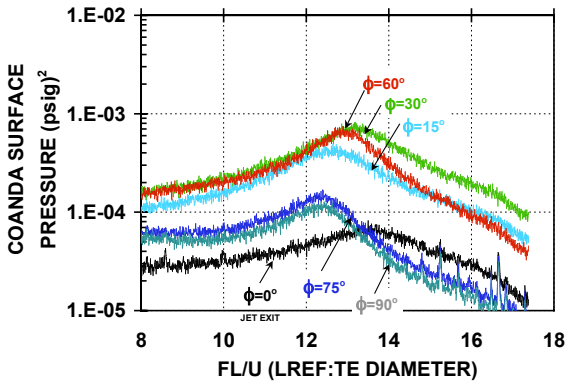

(b) Expanded view of frequency content for the influence of the shear and entrained flow

Figure 57 Frequency content of the pressure field on Coanda surface, steady jet, circular TE, h/C=0.00106

$60<\phi<75$.

The turbulence magnitude and frequency of the jet-on portion of the pulse train increases just downstream of the jet exit, then increases along the Coanda surface to peak at $\phi=60^{o}$ shown in Figure 58. The magnitude and frequency then decays until the jet separates from the Coanda surface between $75<\phi<90$.

The performance benefit of the pulsed elliptic trailing edge is significantly less than that of the circular trailing edge, shown in Figure 59. For a lift coefficient of 1.0 there is a 29% reduction of mass flow for the pulsed elliptic trailing edge compared to the 55% reduction ot the circular trailing edge. There was no measureable benefit in mass flow reduction for the pulsed biconvex

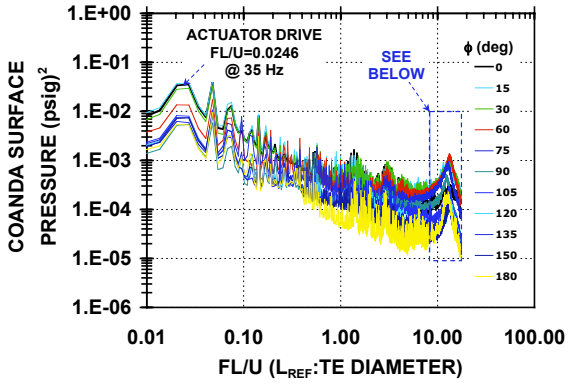

(a) Non-dimensional Spectra for pulsed jet

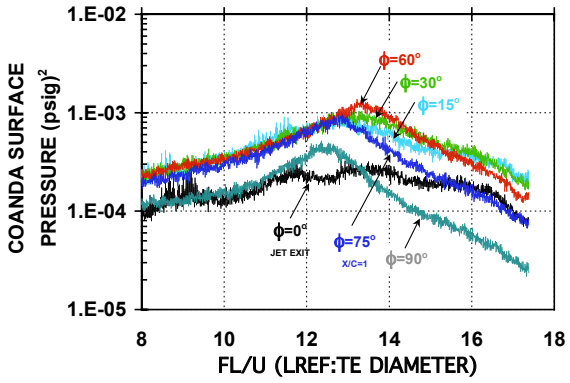

(b) Expanded view of frequency content for the pulse-on portion of pulse train

Figure 58 Frequency content of the pressure field on Coanda surface, actuator drive: 35 Hz, 40% duty cycle, circular TE, h/C=0.00106

trailing edge.

The effectiveness of the pulsed blowing can be related to radius of curvature of the Coanda surface and jet separation. The pulsed effectiveness for larger r/C that is represented by the 2% circular trailing edge, moved the time averaged separation beyond the maximum trailing edge location of x/C=1.0, i.e. from the upper Coanda surface to the lower Coanda surface.

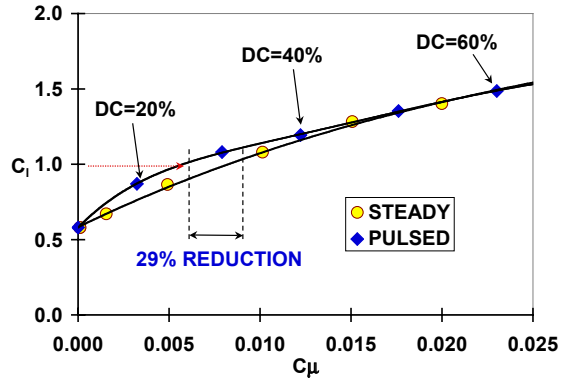

Figure 59 Mass flow reduction for pulsed elliptic trailing edge, h/C=0.0022, boundary layer control region

Several factors contribute to the effectiveness of the pulsed jet, that include a larger instantaneous velocity, the increased turbulence (for mixing), pulse frequency, pulse duty cycle, and the limitation of a steady jet to remain attached to a small radius of curvature. Further research is needed to isolate these parameters.

Concluding Remarks

The efficiency of the GACC airfoil is compared to other CC airfoils in Figure 60. The details of the other CC airfoil data are described in reference 9 and shown here to capture the range of possibilities for the GACC configuration.

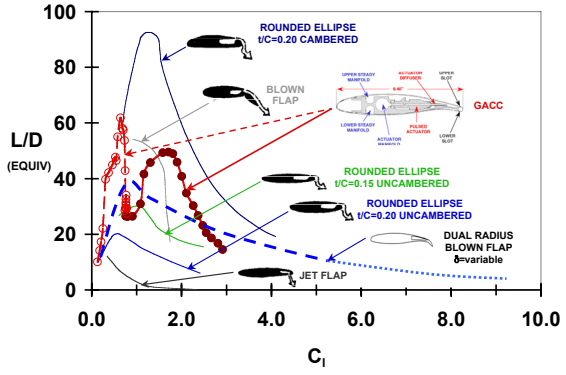

Figure 60 Comparison of GACC efficiency with similar CC airfoils, AOA=0 unless otherwise noted, (curves do not necessarily represent the envelope of maximum efficiency $Cl/Cd_{EQUIVALENT}$)

Comparing the improved efficiency of the cambered rounded ellipse airfoil[21] is believed to be a function of the larger radius of the circular trailing edge used in the elliptical airfoil. The increased efficiency of the camber for the elliptical airfoil is also shown for the t/C=0.20 configuration[21]. The camber effects of the GACC airfoil are demonstrated in the generation of higher lift for comparable momentum coefficients. Comparing the GACC efficiency to a typical blown flap[36] reveals the lift benefit of attaching the jet through Coanda turning. It is speculated that the blown flap prematurely separates, limiting it's lift performance to $C_l<2$. Reshaping the blown flap to the dual radius CC flap profile, enables the jet to remain attached to the trailing edge of the flap, extending it's lift performance to $C_l\approx5$. It should be noted that leading edge blowing was required to extend the lift coefficient beyond $C_l\approx5$ for the dual radius flap[37]., The poor efficiency of the jet flap[38] is generally related to the large blowing requirements associated with the reactionary force, and the minimal effect on the 2D induced pressure field.

The efficiency of the GACC's dual blown configuration highlights the low speed cruise conditions. Nominally the lift requirements for cruise are $C_l\approx0.5$. Recall from Figure 50 that most of the real drag is in the form of thrust. It is also unclear what Ujet to use in the Cμ equation since the upper and lower are controlled independently.

The general performance of the GACC airfoil is good, but has not been tested to it's limits. It is recommended that leading edge active flow control be added to extend the limits of lift. It is also important to extend the pulsed performance benefits into the supercirculation region.

Selecting the GACC airfoil section for use on an ESTOL or PAV vehicle may be premature. It does seem to be an excellent candidate for the outboard portion of the wing., having good lift augmentation capability and good roll and yaw potential.

Appendix

Wall Interference

As a first approximation of the wall interference characteristics, corrections for 2D lift interference can be made using a classic approach described by Krynytzky[39] and Allan and Vincenti[40]. For a small model centrally located between two closed parallel walls, corrections for angle of attack, lift, and pitching moment can be estimated using the following:

$$\Delta\alpha = \frac{\pi c^2}{96\beta H^2}\left(C_L + 4C_M\right) \qquad \text{Equation 23}$$

$$\Delta C_L = -\frac{\pi^2}{48}\left(\frac{c}{\beta H}\right)^2 C_L \qquad \text{Equation 24}$$

$$\Delta C_m = \frac{\pi^2}{192}\left(\frac{c}{\beta H}\right)^2 C_L \qquad \text{Equation 25}$$

$$q_{CORR} = \left[1+\left(2-M^2\right)\varepsilon\right]q_{UNCORR} \qquad \text{Equation 26}$$

where

$$\varepsilon = \varepsilon_{SOLID} + \varepsilon_{WAKE} \qquad \text{Equation 27}$$

and

$$\varepsilon_{SOLID} = \frac{\pi}{6}\left[1+1.2\beta\left(\frac{t}{c}\right)\right]\left[1+1.1\left(\frac{c}{t}\right)\alpha^2\right]\frac{A_0}{\beta^3 H^2}$$

Equation 28

and

$$\varepsilon_{WAKE} = \frac{C_D}{4\beta^2}\left(\frac{c}{H}\right) \qquad \text{Equation 29}$$

Example of the wall interference corrections described by equations 22, 23, and 24 are small as seen in Figure 60, 61, 62, and 63.

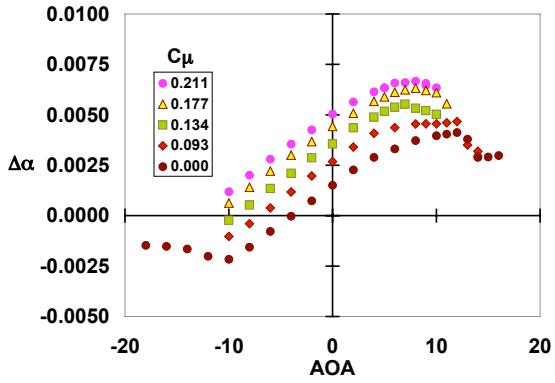

Figure 61 Angle of attack correction from wall interference (circular TE)

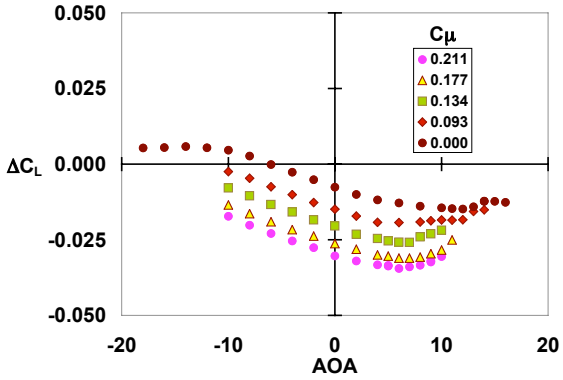

Figure 62 Lift corrections from wall interference (circular TE)

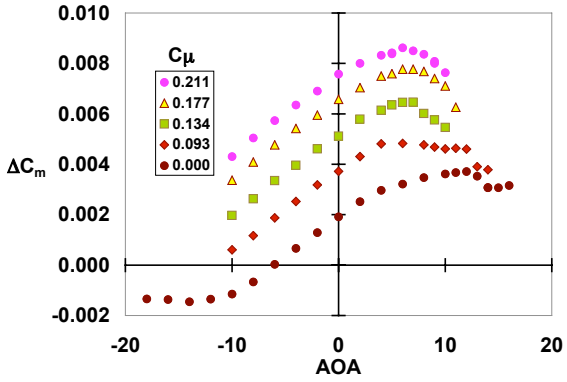

Figure 63 Moment correction from wall interference (circular TE)

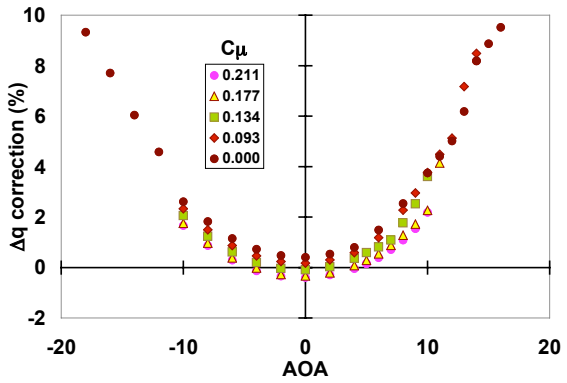

Figure 64 Dynamic pressure correction from wall interference (circular TE)

Balance Corrections

Data reduction equations and tare corrections for pressure lines across balance:

$$NF = \theta_{NF}(NF_{SC}) - \sum(NF_{INTERACTIONS})$$

$$AF = \theta_{AF}(AF_{SC}) - \sum(AF_{INTERACTIONS} + PressureCorrection)$$

$$PM = \theta_{PM}(PM_{SC}) - \sum(PM_{INTERACTIONS} + PressureCorrection)$$

$$YM = \theta_{YM}(YM_{SC}) - \sum(YM_{INTERACTIONS} + PressureCorrection)$$

$$RM = \theta_{RM}(RM_{SC}) - \sum(RM_{INTERACTIONS})$$

Pressure tare correction for axial, pitching moment, and yawing moment forces:

$$AF_{LOAD} = (AF_{LOAD})_{CALCULATED} + \sum(PRESSURE\ TARE_{CORRECTION})$$

where

$$PRESSURE\ TARE_{CORRECTION} = J_1P_{ACT} + J_2P_{UPPER} + J_3P_{LOWER} + J_4P_{ACT}P_{UPPER} + J_5P_{ACT}P_{LOWER}$$

$$PM_{LOAD} = (PM_{LOAD})_{CALCULATED} + \sum(PRESSURE\ TARE_{CORRECTION})$$

where

$$PRESSURE\ TARE_{CORRECTION} = K_1P_{ACT} + K_2P_{UPPER} + K_3P_{LOWER} + K_4P_{ACT}P_{UPPER} + K_5P_{ACT}P_{LOWER}$$

$$YM_{LOAD} = (YM_{LOAD})_{CALCULATED} + \sum(PRESSURE\ TARE_{CORRECTION})$$

where

$$PRESSURE\ TARE_{CORRECTION} = I_1P_{ACT} + I_2P_{UPPER} + I_3P_{LOWER} + I_4P_{ACT}P_{UPPER} + I_5P_{ACT}P_{LOWER}$$

The accuracy of the balance is highlighted in table 2. The rolling moment and yawing moments are meaningless for 2-D testing and will be ignored except in when calculating the interactions to obtain corrected Normal, Axial, and Pitching moments.

Normal (%FS)	Axial (%FS)	Pitching Moment (%FS)	Rolling Moment (%FS)	Yawing Moment (%FS)
0.04	0.39	0.12	0.07	1.64

Table 2 GACC Strain gage balance accuracy (95% confidence level)

References

[1] Jones, G.S., Joslin, R.D., "NASA/ONR 2004 Circulation Control Workshop", Oral presentation, Hampton, VA. March 2004.

[2] McKinley, R,J., "Future Vehicle Capabilities & the Potential Contribution of Circulation Control", NASA CP xxxx, pg x-x, March 2004.

[3] Moore, M.D., "Wake Vortex Wingtip-Turbine Powered Circulation Control High-Lift System" ", NASA CP xxxx, pg x-x, March 2004.

[4] Wood, N., and J. Nielson, "Circulation Control Airfoils Past, Present, and Future," AIAA Paper 850204, January,1985.

[5] Englar, R.J., Circulation control Pneumatic Aerodynamics: blown force and Moment Augmentation and Modifications; Past, Present, & Future", AIAA 2000-2541, June 2000

[6] Jones, G.S., Bangert, L.S., Garber, D.P., Huebner, L.D., McKinley, R.E., Sutton, K., Swanson, R.C., Weinstein, L., "Research Opportunities in Advanced Aerospace Concepts", NASA TM-2000-210547, December 2000

[7] Davenport, F. J., "A Further Discussion of the Limiting Circulatory Lift of a Finite-Span Wing," J. of the Aerospace Sciences, Dec. 1960, pp. 959-960.

[8] Smith, A.M.O., "High-Lift Aerodynamics," J. Aircraft, Vol. 12, No. 6, June 1975

[9] Wilson, M.B., von Kerczek, C., "An Inventory of Some Force Producers for use in Marine Vehicle Control", DTNSRDC-79/097, November 1979

[10] Schlichting, H., "Boundary Layer Theory", 6th ed. N.Y., McGraw-Hill, 1968

[11] Rae, W.H., Pope, A., "Low-Speed Wind Tunnel Testing", 2nd Edition, John Wiley & Sons, 1984

[12] Kind, R.J., "A Proposed Method of Circulation Control", University of Cambridge Ph.D. Thesis, June 1967

[13] Englar, R. J., Williams, R.M., "Test Techniques for High Lift, Two-Dimensional Airfoils with Boundary Layer and Circulation Control for Application to Rotary Wing Aircraft", Canadian Aeronautics and Space Journal, vol. 19, no. 3, March 1973

[14] Jones, G.S., Viken, S.A., Washburn, A.E., Jenkins, L.N., & Cagle, C.M., "An Active Flow Circulation Controlled Flap Concept for General Aviation Applications", AIAA 2002-3157, June 2002

[15] Lan, C.E. and Roskam, J., "Airplane Aerodynamics and Performance," Published by Roskam Aviation and Engineering, 1981

[16] Horner, "Aerodynamic Lift",

[17] Raymer, D.P., "Aircraft Design: A Conceptual Approach," AIAA Education Series, 3rd Edition, 1999

[18] McGhee, R.H. and Bingham, G.H., "Low-Speed Aerodynamic Characteristics of a 17-Percent Thick Supercritical Airfoil Section, Including a Comparison Between Wind-Tunnel and Flight Data," NASA TM X-2571, July 1972

[19] Cagle, C.M., Jones, G.S., "A Wind Tunnel Model to Explore Unsteady Circulation Control for General Aviation Applications", AIAA 2002-3240, June 2002

[20] Englar, R.J., "Low Speed Aerodynamic Characteristics of a Small Fixed Trailing Edge Circulation Control Wing Configuration Fitted to a Supercritical Airfoil", Report number DTNSRDC/ASED-81/08, March 1981

[21] Englar, R.J., and Williams, R.M., "Design of Circulation Controlled Stern Plane for Submarine Applications," David Taylor Naval Ship R&D Center Report NSRDC/AL-200 (AD901-198), March 1971

[22] Englar, R.J., et.al., "Design of the Circulation Control Wing STOL Demonstrator Aircraft," AIAA Paper No. 79-1842 presented at the AIAA Aircraft Systems and Technology Meeting, New York (Aur 1979). Republished in AIAA Journal of Aircraft, Vol. 18, No.1, pp. 51-58 (Jan 1981)

[23] Pugliese, A.J. and Englar, R.J., "Flight Testing the Circulation Control Wing," AIAA Paper No 79-1791 presented at AIAA Aircraft Systems and Technology Meeting, New York (Aug 1979)

[24] Rae, W.H., Jr., Pope, A. "Low-Speed Wind Tunnel Testing", 2nd Edition, John Wiley & Sons, 1984

[25] Preller, R.F., Rose, O.J., "Langley Wind Tunnel Force Reduction Program," NASA CR-165650, November 1980

[26] Smith, D.L., "An Efficient Algorithm using Matrix Methods to Solve Wind Tunnel Force-Balance Equations," NASA-TN-D-6860, August 1972

[27] Ewald, B.F.R. (editor), Wind Tunnel Wall Correction, AGARDograph 336, October 1998

[28] Iyer, V., Kuhl, D.D., and Walker, E.L., "Improvements to Wall Corrections at the NASA Langley 14X22-FT Subsonic Tunnel", AIAA 2003-3950, June 2003

[29] Englar, R.J., NSRDC Technical Note AL-211 (1971)

[30] Lawford, J.A. and Foster, D.N., "Low-Speed Wind-Tunnel Tests on a Wing Section with Plain Leading and Trailing-Edge Flaps Having Boundary-Layer Control by Blowing", British aeronautical Research Council R&M 3639 (1970)

[31] Alvarez-Calderon, A., and Arnold, F.R., "A study of the Aerodynamic Characteristics of a High-Lift Device Based on a Rotating Cylinder and Flap," Stanford-University, Department of Mechanical engineering Technical Report RCF-1 (1961)

[32] Rose, R.E., Hammer, J.M., & Kizilos, A.P., "Feasibility Study of a Bi-directional Jet Flap Device for Application to Helicopter Rotor Blades," Honeywell Document No. 12081-FR1, July 1971

[33] Rogers, E.O., Donnelly, M.J., "Characteristics of a Dual-Slotted Circulation Control Wing of Low Aspect Ratio Intended for Naval Hydrodynamic Applications," AIAA 42nd Aerospace Sciences Meeting, Reno, NV, 5-8 Jan 2004 AIAA 2004-1244

[34] Oyler, T.E., Palmer, W.E., "Exploratory Investigation of Pulse Blowing for Boundary Layer Control", North American Rockwell Report NR72H-12, January 15, 1972

[35] Walters, R.E., Myer, D.P., & Holt, D.J., "Circulation Control by Steady and Pulsed Blowing for a Cambered Elliptical Airfoil", West Virginia University, Aerospace Engineering TR-32, July 1972

[36] Lawford, J.A., and Foster, D.N., "Low-Speed Wind Tunnel Tests on a Wing Section with Plain Leading- and Trailing-Edge Flaps Having Boundary-Layer Control by blowing," British Aeronautical Research Council R&M 3639 (1970)

[37] Englar, R.J., Huson, G.G., "Development of Advanced Circulation Control Using High-Lift Airfoils," AIAA Paper No. 83-1847, July 13-15, 1983

[38] Williams, J. and Alexander, "Some Exploratory Three-Dimensional Jet-Flap Experiments," Aeronautical Quarterly, Vol. 8, pp 21-30 (1957)

[39] Krynytzky, A., & Hackett, J.E., "Choice of Correction Method", Section 1.4, AGARDograph 336, October 1998

[40] Allan, H.J., and Vincenti, W.G., "Wall Interference in a Two-Dimensional-Flow Wind Tunnel with Consideration of the Effect of Compressibility, NACA Report 782, 1944

Pneumatic Flap Performance for a 2D Circulation Control Airfoil

Greg Jones, Ph.D.
Flow Physics and Control Branch
NASA Langley Research Center

OBJECTIVES

- Establish Baseline Performance of GACC (Steady blowing)
  - HIGH LIFT (upper Coanda blowing - TARGET $C_{LIFT} = 3$)
  - CRUISE (pneumatic flap - dual blowing to Reduce Cruise Drag associated with blunt trailing edge)
- Determine the Performance benefits of Pulsed CC
  - Actuator Performance
  - Model Performance
- Evaluate Trailing Edge Shape
  - Circular
  - 2:1 Elliptic
  - 2:1 Biconvex

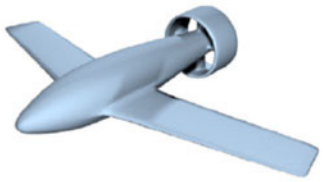

GACC DESIGN

Multi-Functional Configurations
Upper Blowing : High Lift
Lower Blowing : Flight Control
Dual Blowing : Cruise
Pulsed Blowing : Economic Control
Distributed Blowing: Load Control

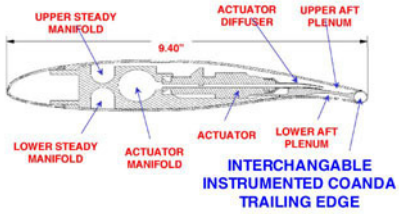

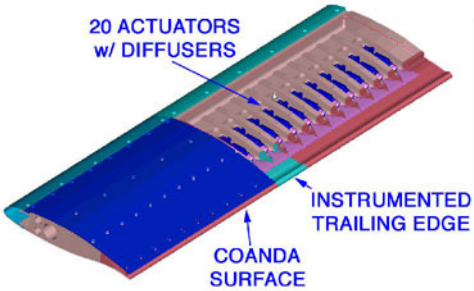

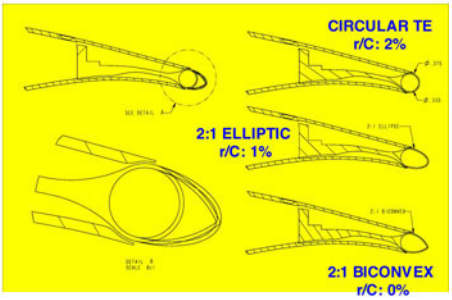

BART SETUP

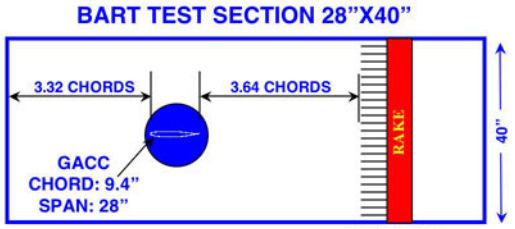

Model Setup

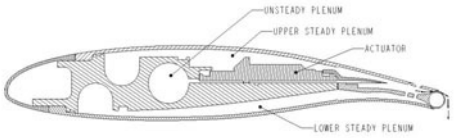

UNSTEADY
P+p'

LEADING EDGE MEMS (21)
TE MEMS INBOARD (15)
TE MEMS OUTBOARD(15)
TE REF (ENDEVCO) (4)
INTERNAL MODEL MEMS (1)

UNSTEADY
E+e'

TE HOT FILMS INBOARD (21)
TE HOT FILMS OUTBOARD(21)
TE REF (ENDEVCO) (4)
INTERNAL MODEL MEMS (1)

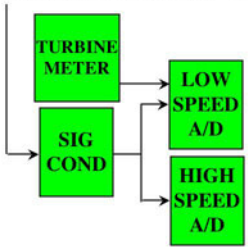

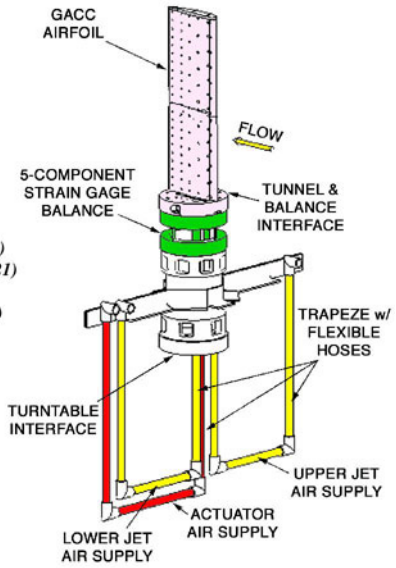

MASS FLOW CONSIDERATIONS

$$C\mu = \frac{\text{Thrust}}{qS} = \frac{\dot{m}(U_J)}{q(C)(b)} \qquad U_J = \sqrt{\frac{2\gamma R(T_{DUCT})}{\gamma - 1}\left(1 - \left(\frac{P_\infty}{P_{DUCT}}\right)^{\frac{\gamma-1}{\gamma}}\right)}$$

$$C\mu = 2\left[\frac{(h)(w)}{(C)(b)}\right]\left(\frac{\rho_J}{\rho_\infty}\right)\left(\frac{U_J}{U_\infty}\right)^2$$

$$C_d = C_{d_{rake}} - \frac{\dot{m}V_\infty}{q\,S}$$

$$= C_{d_{rake}} - C_\mu \frac{V_\infty}{V_j}$$

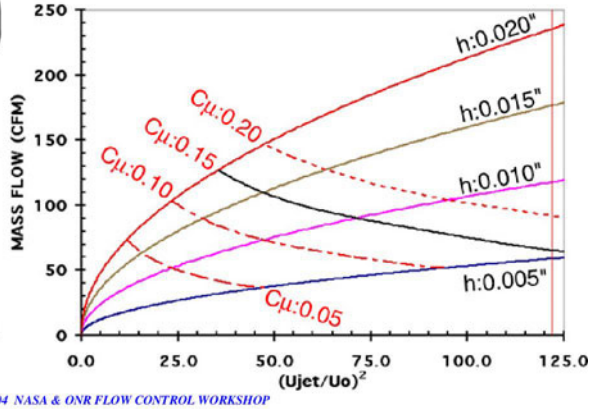

MOMENTUM INFLUENCE ON DRAG

$$C_{D(EQUIV)} = C_{D(BAL)} + C\mu\left(\frac{U_J}{2U_\infty}\right) + C\mu\left(\frac{U_\infty}{U_J}\right)$$

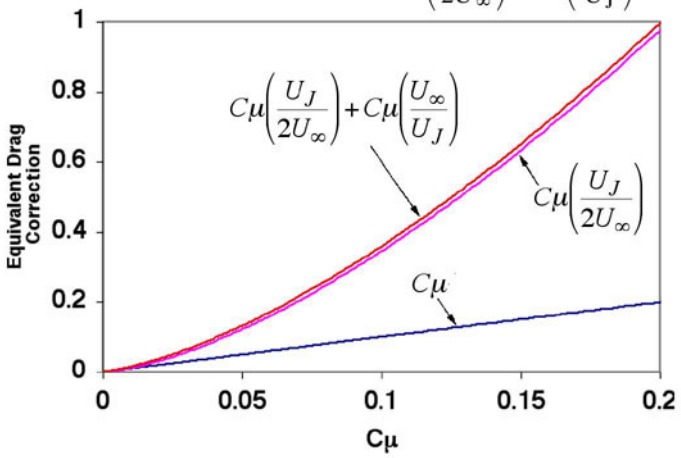

GACC - 2D Airfoil
General Aviation Circulation Control

CFD - FUN(2D)

Mach: 0.1 AOA: 0.0°

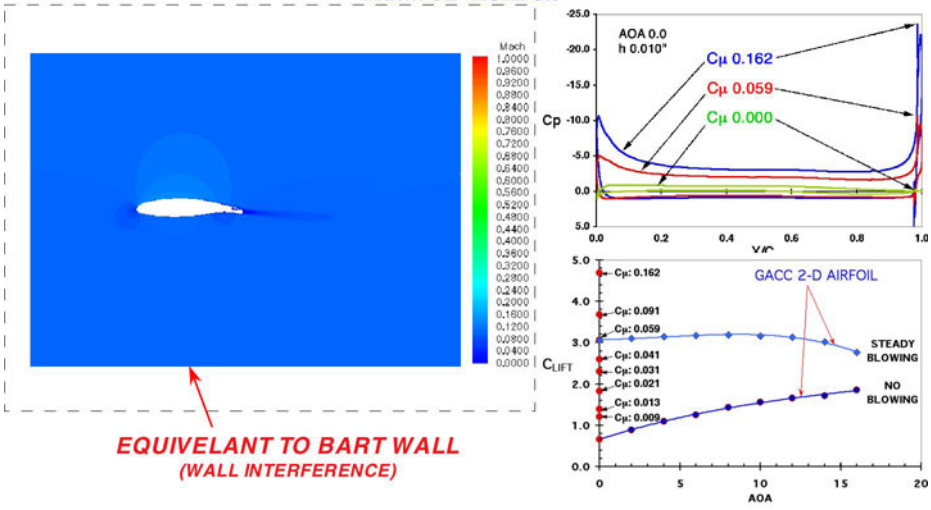

EQUIVELANT TO BART WALL
(WALL INTERFERENCE)

2004 NASA & ONR FLOW CONTROL WORKSHOP

CFD - FUN(2D)

Trailing Edge & Slot Data

h: 0.010" h/R: 0.0533 h/C: 0.001 R/C: 0.02

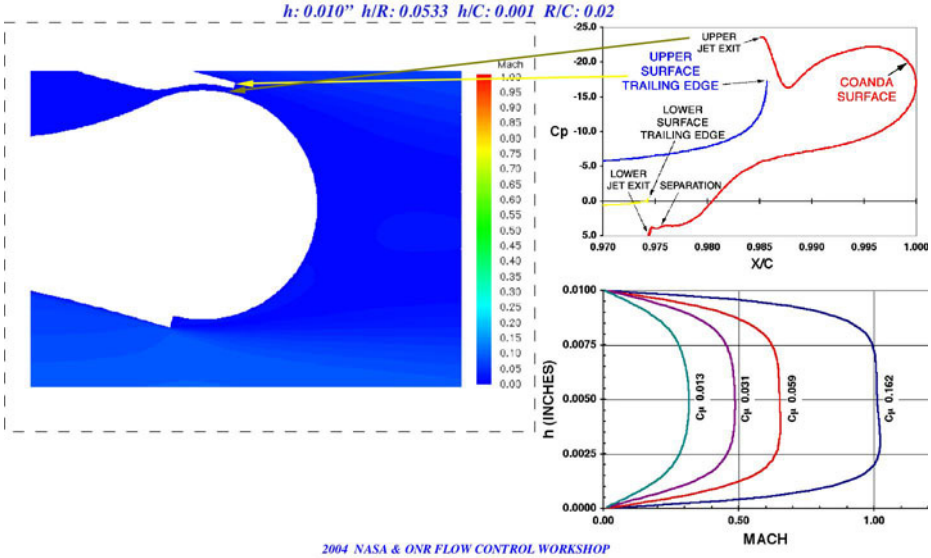

LIFT PERFORMANCE

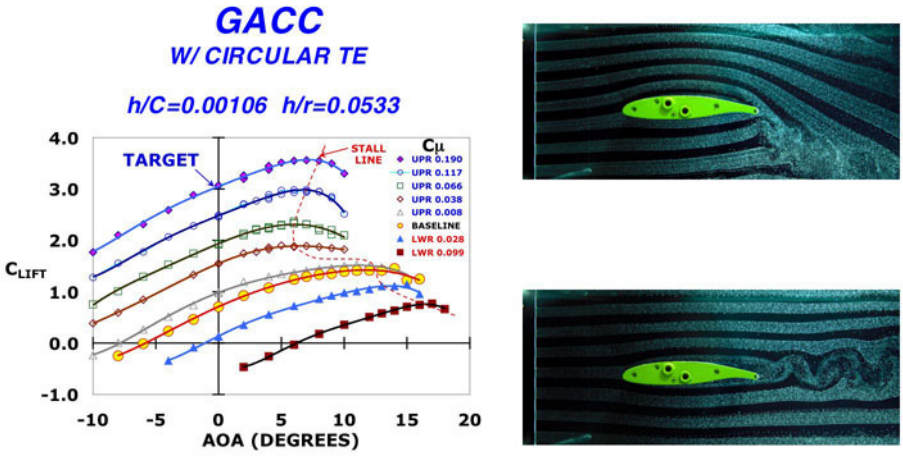

Circular TE - Compare h

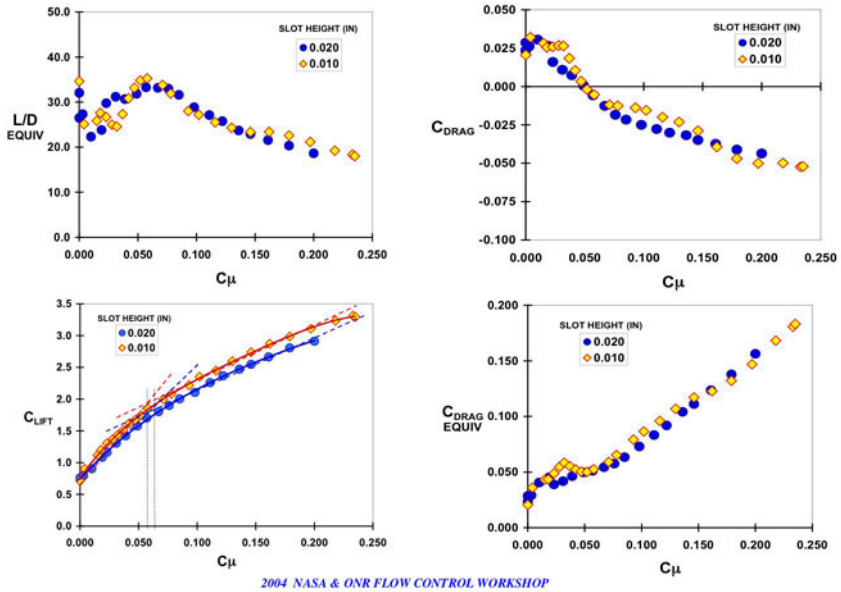

WAKE - Steady Blowing

PRESSURE PROFILES
(3.6 CHORDS DOWNSTRAM OF TE)

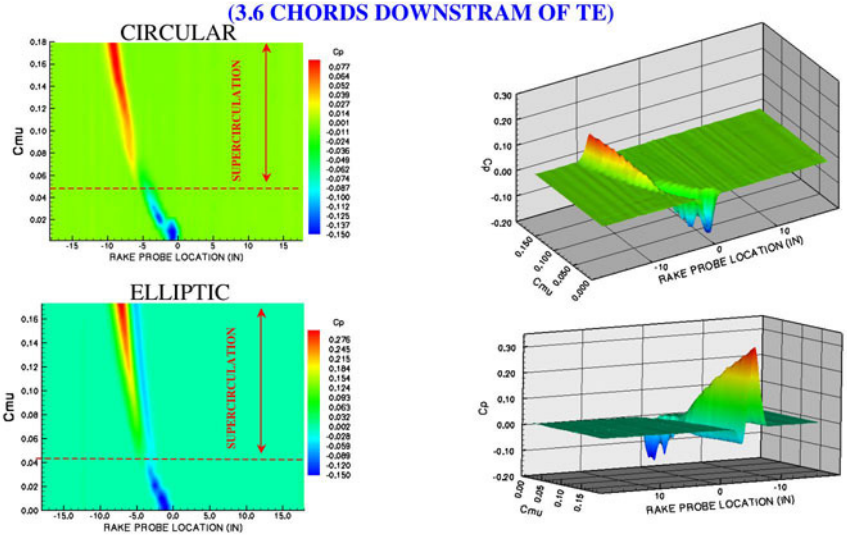

NOSE UP PITCHING MOMENT

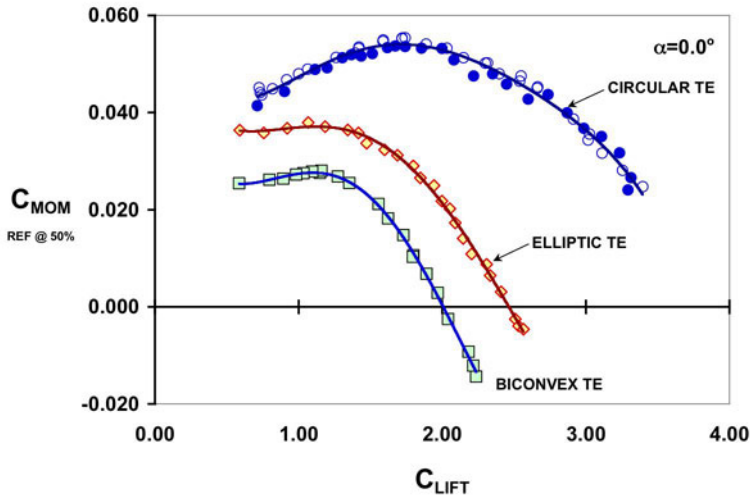

Pitching Moment

BALANCE DATA for CIRCULAR COANDA TE

REF: 25% CHORD

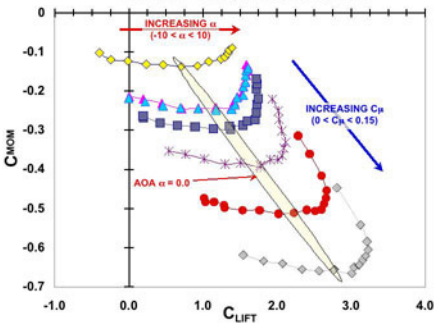

REF: 50% CHORD

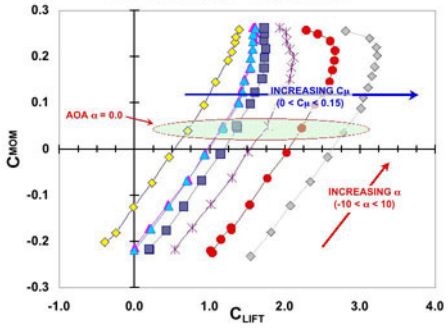

PRESSURE DISTRIBUTION

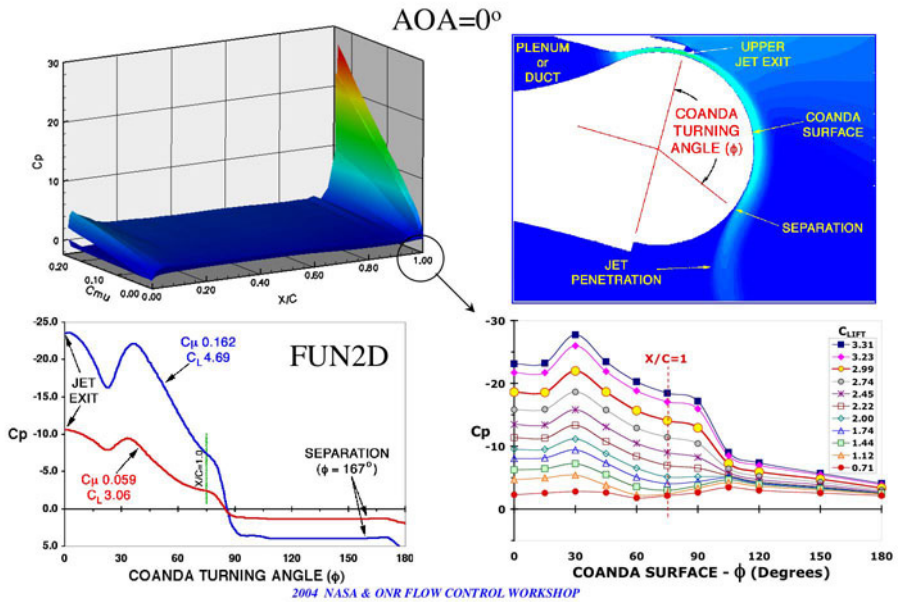

LIFT AUGMENTATION

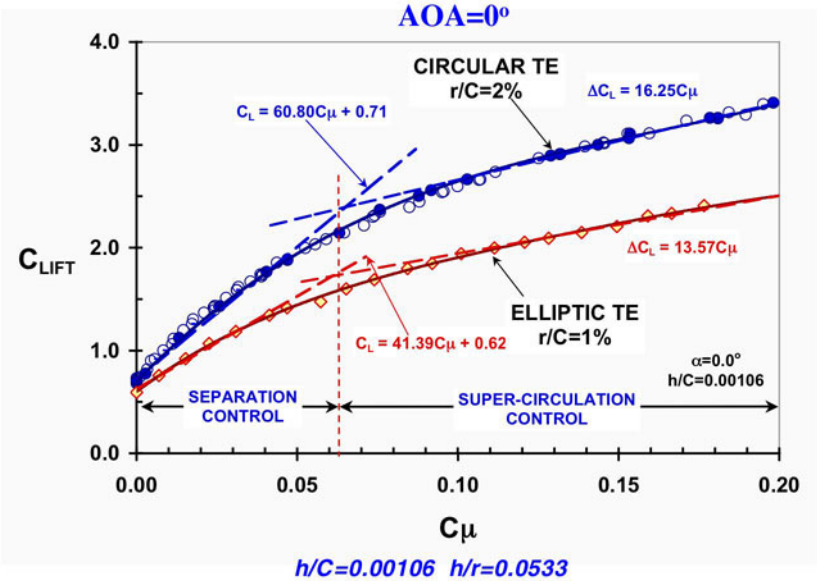

GACC - 2D Airfoil
General Aviation Circulation Control

TE SEPARATION

GACC w/ Tufts

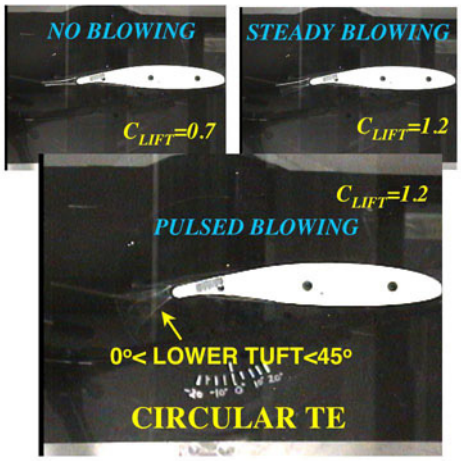

35 Hz & 40% DUTY CYCLE

Mass Flow Reduction = 45%

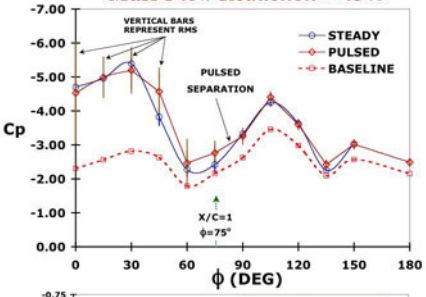

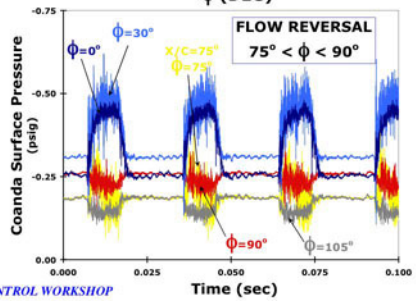

GACC - 2D Airfoil
General Aviation Circulation Control

Elliptic TE - Steady & Pulsed

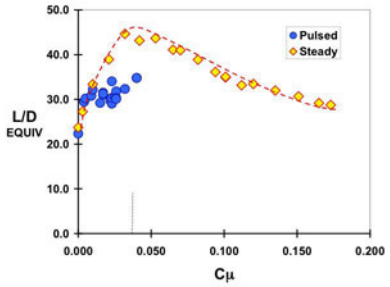

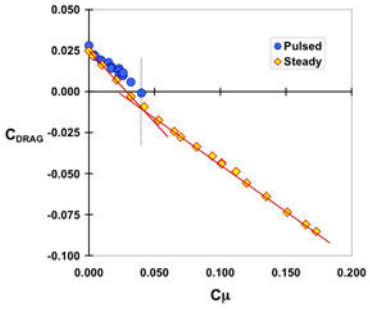

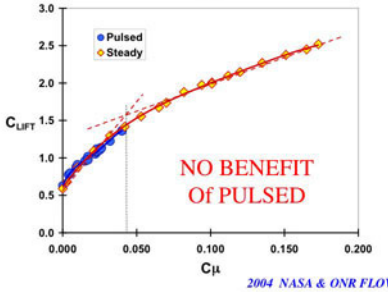

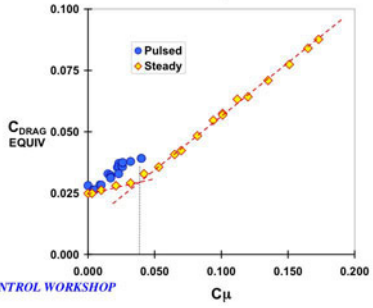

Circular TE - Steady & Pulsed

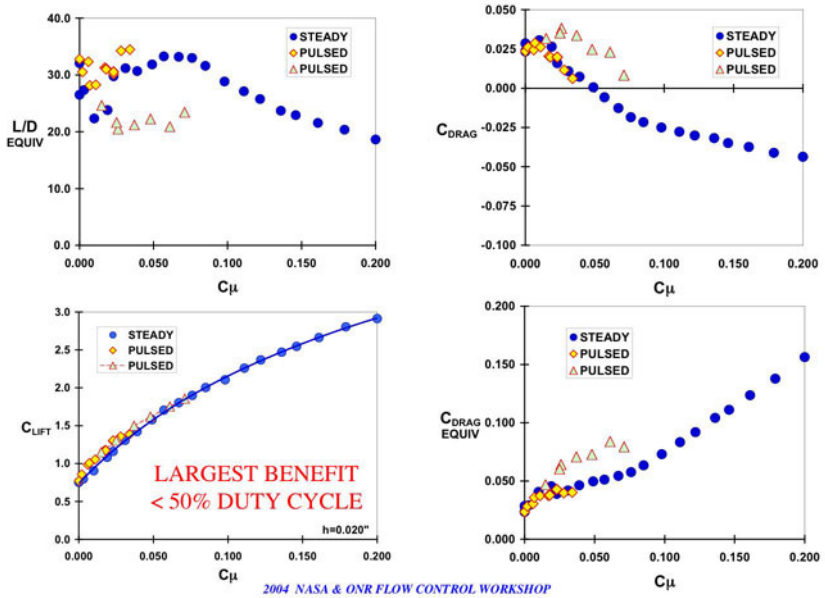

PULSED BLOWING

CIRCULAR TE PERFORMANCE BENEFIT

IN SEPARATION CONTROL REGION

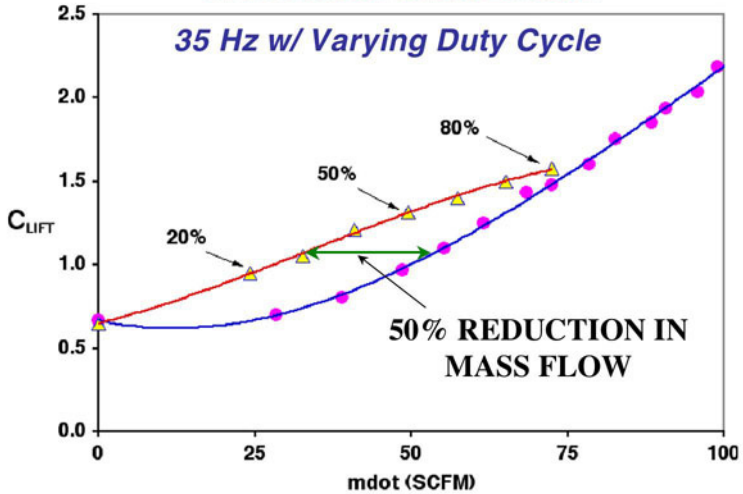

Elliptic TE - Dual Blowing

$C\mu = C\mu_{UPPER} + C\mu_{LOWER}$

$C\mu_{UPPER} = C\mu_{LOWER}$

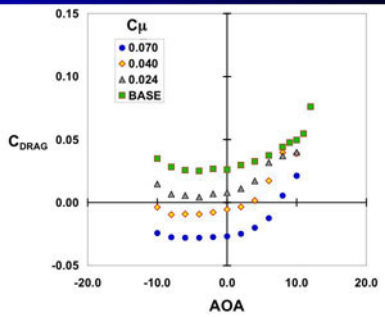

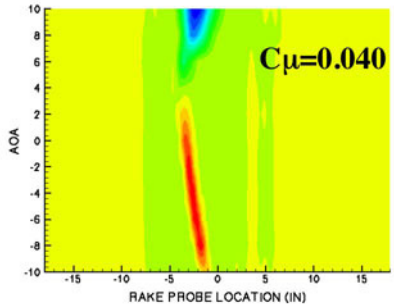

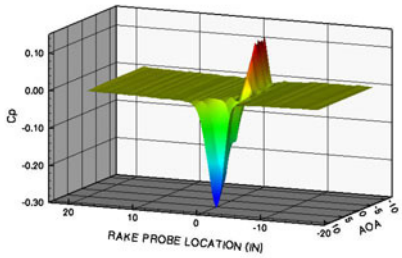

Dual Blowing Performance

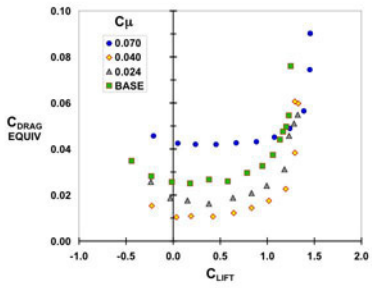

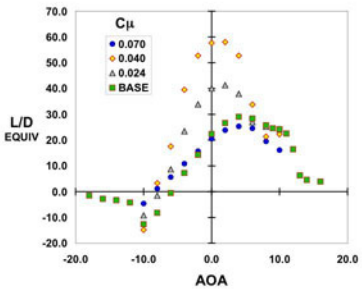

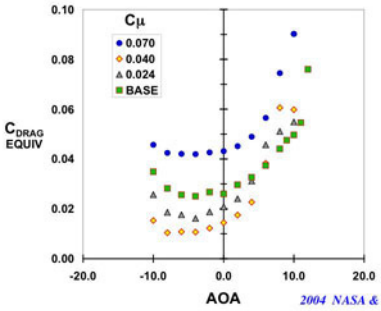

Over Blowing Results
In Increased Equivalent
Drag but Increased Thrust

OBSERVATIONS

- CIRCULAR TE PRODUCED MORE LIFT THAN ELLIPTIC OR BICONVEX TE
  - r/C EFFECT
- ELLIPTIC TE PRODUCED LESS DRAG THAN CIRCULAR TE
- WAKE RAKE WAS MORE RELIABLE THAN FORCE BALANCE IN DETERMINING DRAG
  - JUNCTURE FLOW INFLUENCE (NO SIDEWALL BLOWING)
- PULSED BLOWING WAS EFFECTIVE ON CIRCULAR TE BUT NOT ELLIPTIC OR BICONVEX TE
  - ACTUATOR AUTHORITY NOT ENOUGH TO ACHIEVE SUPERCIRCULATION
- ERRORS IN SETTING SLOT HEIGHT PROPOGATE THRU $C\mu$ THEN $C_{DRAG(EQUIV)}$

GACC - 2D Airfoil
General Aviation Circulation Control

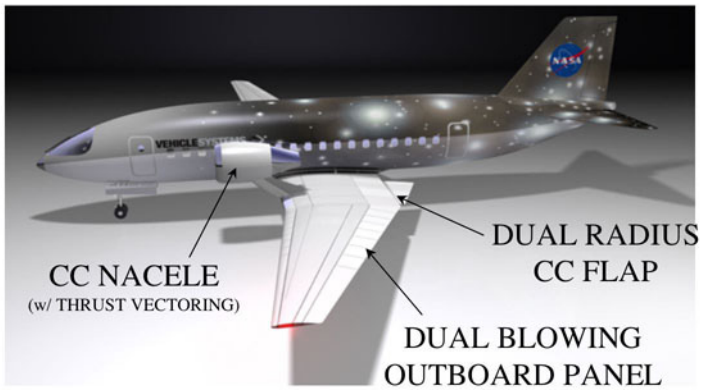

2004 NASA & ONR FLOW CONTROL WORKSHOP

BACKUP SLIDES

BART Video

Baseline Performance

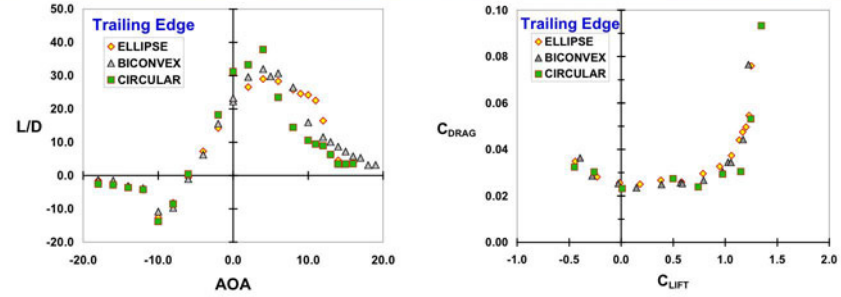

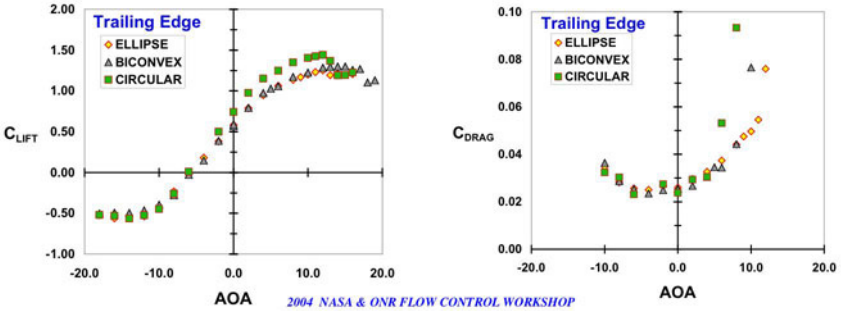

Elliptic TE - Pulsed Blowing